https://doi.org/10.5194/egusphere-2026-1890
Preprint. Discussion started: 14 April 2026

Characterization and correction of detector nonlinearity in Fourier-transform interferograms

Bavo Langerock[1], Minqiang Zhou[2], Martine De Mazière[1], Mahesh Kumar Sha[1], Filip Desmet[1], Bart Dils[1], Corinne Vigouroux[1], Rigel Kivi[3], Isamu Morino[4], Mathias Palm[5], Gopala Krishna Darbha[6], Soumik Banerjee[6], Sujata Ray[6], and Mohmmed Talib[6]

[1]Royal Belgian Institute for Space Aeronomy, Ringlaan 3, 1180 Ukkel, Belgium
[2]Institute of Atmospheric Physics, Chinese Academy of Sciences, Beichenxilu-81, Beijing 100029, China
[3]Space and Earth Observation Centre, Finnish Meteorological Institute, Tähteläntie 62, 99600 Sodankylä, Finland
[4]National Institute for Environmental Studies, Onogawa 16-2, Tsukuba 305-8506, Japan
[5]Institute of Environmental Physics, University of Bremen, Otto-Hahn-Allee 1, 28359 Bremen, Germany
[6]Indian Institute of Science Education and Research Kolkata, Mohanpur, West Bengal, India

Correspondence: B. Langerock (bavo.langerock@aeronomie.be)

Abstract. Atmospheric gas products obtained from remote sensing observational networks operating groundbased FTIR interferometers such as COCCON, NDACC and TCCON are known to be sensitive to nonlinear detector response. Existing methods to correct interferograms for nonlinear detector response showed that the effect of the correction on the retrieved atmospheric gas concentrations can exceed the reported uncertainties on these data products. Several methods to correct the recorded interferograms or spectra exist but turned out to have only a limited applicability mainly due to underlying assumptions. A new nonlinearity characterization method is presented which builds upon previous methods and overcomes most assumptions on the underlying measurement setup. The method is demonstrated on five distinct nonlinearity episodes for measurements obtained from two TCCON instruments, one COCCON low-spectral-resolution instrument and one NDACC instrument and includes a study on the effect of the nonlinearity correction on the atmospheric trace gas products derived from these measurements. For the TCCON instruments the new method is compared to the standardized TCCON nonlinearity correction method. New diagnostic metrics that quantify nonlinearity strength are introduced and these are shown to have the potential to characterize the cause of the underlying detector nonlinearity response, being either saturation or optical misalignment.

1 Introduction

Fourier-transform infrared (FTIR) spectrometers have a long history in measuring atmospheric trace gas concentrations. The Network for the Detection of Atmospheric Composition Change (NDACC, De Mazière et al. (2018); Petropavlovskikh et al. (2026)) uses FTIR spectrometers with a high spectral resolution of approximately 0.005 cm^{-1} in order to provide vertically resolved trace gas abundances. The Total Carbon Column Observing Network (TCCON) operates the same FTIR instruments recording at a lower spectral resolution of 0.02 cm^{-1} to provide vertically integrated dry-air mole fractions (DMF) of long-lived greenhouse gases (CO_2, CH_4, N_2O), H_2O, CO, and HF (Wunch et al., 2011, 2015). During recent years it has been demonstrated that FTIR spectrometers with a low spectral resolution ranging from 0.2 cm^{-1} to 0.5 cm^{-1} also have the ability

https://doi.org/10.5194/egusphere-2026-1890
Preprint. Discussion started: 14 April 2026

to provide DMF data with a quality comparable to TCCON data (Frey et al., 2019; Sha et al., 2020). The COllaborative Carbon Column Observing Network (COCCON) is dedicated to DMF retrievals of CO_2, CH_4 and CO from low spectral resolution measurements (Frey et al., 2019). Within these three networks, the atmospheric trace gas concentrations are retrieved from the spectra that are obtained through Fourier transformation of the recorded interferograms. It has been demonstrated that nonlinear detector response leads to distortions in the recorded interferograms and these may cause significant errors in the atmospheric gas retrievals derived from the resulting spectra (Hase, 2000; Sha et al., 2020; Heikkinen and Kivi, 2023; Laughner et al., 2024). Detector nonlinearity will have the largest impact in the center burst region of the interferogram, close to the zero optical path difference (ZOPD) where variations in the recorded signal intensity are high. The spectrum is degraded by changes in the envelope (zero-level) and by out-of-band spectral artifacts (Chase, 1984; Abrams et al., 1994; Hase, 2000). This paper describes in detail a nonlinearity correction method applicable to measurements recorded in the framework of NDACC, TCCON and COCCON and studies the effect of the nonlinearity correction on the retrieved trace gas columns. It is important to mention that the absolute calibration of the recorded intensities or spectral radiances is not relevant for the retrieval of atmospheric gases from the spectra recorded in these networks. This simplifies to some extent the underlying complexity of the nonlinearity correction method presented here.

Most commonly used nonlinearity correction methods rely on the assumption that the distorted recorded AC interferogram I_m can be related to the "true" interferogram I_t corresponding to a linear detector response (Chase, 1984; Abrams et al., 1994; Lachance, 2000; Hase, 2000):

$$I_m = I_t + aI_t^2 + bI_t^3 + \cdots = p(I_t). \tag{1}$$

The power series p on the right-hand side should be applied pointwise on the values in the interferogram (the time/spatial domain of the interferogram). The coefficients $a, b, \ldots$ are constant in time, i.e. they do not vary with the position in the interferogram sequence. p has a special form: there is no scalar term and the coefficient of the first order term is equal to one: $p(x) = x + ax^2 + bx^3 + \cdots, x \in \Re$. A power series of this particular form (no scalar term and a non-zero first order coefficient) allows an explicit formulation for the coefficients of the inverse infinite power series $p^{-1}(x) = x + a'x^2 + b'x^3 + \cdots$, with $a' = -a$, $b' = 2a^2 - b$, … (Morse and Feshbach, 1953; Weisstein, 2026). The relationship in Eq. (1) can therefore be reformulated in its inverse form $I_t = p^{-1}(I_m) = I_m + a'I_m^2 + b'I_m^3 + \cdots$, expressing the true interferogram in terms of the measured distorted one. Nonlinearity correction methods typically provide a method to estimate a finite order approximation of p^{-1}. Such an estimate is known as a nonlinearity *characterization* (Lachance, 2000). The obvious next step that calculates a "corrected" interferogram $I_c \approx I_t = p^{-1}(I_m)$ is called the nonlinearity *correction* (Abrams et al., 1994; Lachance, 2000).

In existing nonlinearity characterizations it is standard to translate the polynomial relationship in Eq. (1) from the time domain to the spectral domain. In FTIR spectrometry one applies the real-to-complex discrete Fourier transform (DFT) to the measured interferogram I_m to obtain a complex spectrum $S_m = \mathrm{DFT}(I_m)$. The polynomial relationship in Eq. (1) is preserved under the DFT but, as a consequence of the convolution theorem (McClellan et al., 2016) the powers of the interferogram become convolution products:

$$S_m = S_t + a(S_t \otimes_N S_t) + b(S_t \otimes_N S_t \otimes_N S_t) + \cdots, \tag{2}$$

https://doi.org/10.5194/egusphere-2026-1890
Preprint. Discussion started: 14 April 2026

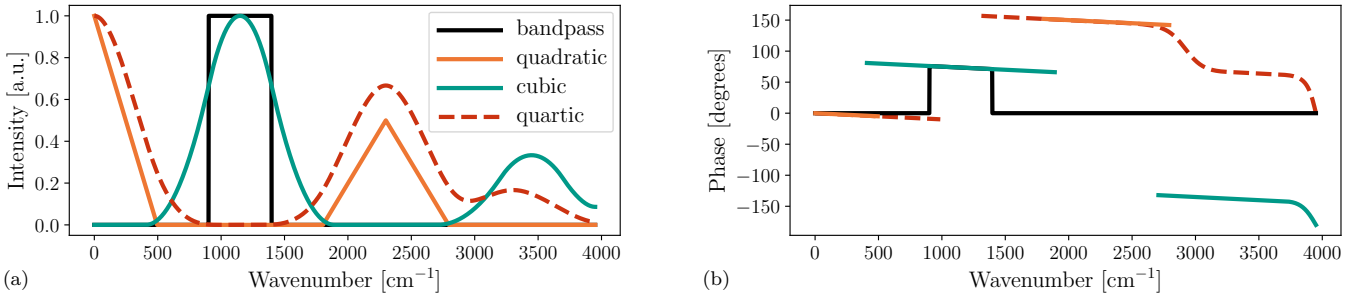

Figure 1. Spectral autocorrelations for a small idealized bandpass window whose position coincides with typical NDACC MCT measurements. (a) Normalized autocorrelations of the idealized bandpass, the maximal intensities decrease for each order $n = 2, 3, 4$ with a factor of approximately $1/10^{n-1}$. For visualization the magnitudes are normalized to have their maximum at 1. (b) Phase sequences for the autocorrelations from (a) when the ideal bandpass is given a linear phase similar to what is encountered in measurements (phase is shown only where the autocorrelation is not zero).

with DFT$(I_t) = S_t$ and $\otimes_N$ the N-point circular convolution operator, N being the number of points in the interferogram (McClellan et al., 2016). This convolution operator is explained in more detail in Sec. 2. The autocorrelation terms appearing in the right-hand side of Eq. (2) are responsible for the nonlinearity spectral features, called the quadratic, cubic, ... artifacts. Figure 1(a) shows such autocorrelations for an idealized bandpass centered at 1150 cm^{-1} in a typical spectrum recorded with a Mercury Cadmium Telluride (MCT) detector in an FTIR spectrometer configured for NDACC-type operations. Lachance (2000) mentions that for sufficiently small bandwidths, i.e. the range of frequencies passing the optical filter, the dominating quadratic spectral artifact does not overlap with the spectral in-band region. Cubic artifacts however always overlap with the in-band spectral range. They play a role in measurements affected by strong nonlinearity where the cubic term is not negligible. Spectra recorded with MCT and InSb (Indium Antimonide) detectors in the framework of the NDACC use a small optical bandwidth filter and the in-band region is therefore only affected by cubic (stronger) nonlinearity artifacts (typical NDACC bandwidth is of the order of 1000 to 3000 wavenumbers). This is different for measurements from the TCCON or COCCON with a wide bandpass determined by the InGaAs (Indium Gallium Arsenide) detector spectral response region. They are more sensitive to nonlinearity errors and examples of nonlinearity correction will therefore mainly focus on measured interferograms in the TCCON and COCCON recorded with an InGaAs detector. The latest TCCON processor imposes a threshold on nonlinearity strength and this additional quality filter causes gaps in several stations DMF time series (Laughner et al., 2024). An improved nonlinearity correction method is therefore essential for the TCCON.

The nonlinearity characterization or estimation of coefficients for p^{-1} presented in this paper relies on the same underlying idea as in Knuteson et al. (2004). We estimate the coefficients of the polynomial p using a fitting algorithm on the out-of-band spectral artifacts in the measured spectrum. In the right-hand side of Eq. (2), the unknown true spectrum is substituted with the measured spectrum restricted to the in-band region. Here the key assumption is that the quadratic or cubic spectral artifacts in the in-band region are much smaller than the actual spectral signal and will not significantly contribute to the higher order autocorrelations. Several nonlinearity characterization methods have been developed previously relying on this

https://doi.org/10.5194/egusphere-2026-1890
Preprint. Discussion started: 14 April 2026

assumption (Knuteson et al., 2004; Qi et al., 2020; Han, 2018; Guo et al., 2024). These methods estimate the quadratic term in p^{-1} and take into account the DC-level of the recorded interferogram. On the one hand we extend these methods by including estimation of the cubic coefficient, which increases complexity. On the other hand, since the absolute calibration of the spectra is not relevant for measurements obtained from the three ground-based networks under consideration, some technical aspects can be left out which reduces complexity.

Section 2 describes the method to estimate the polynomial coefficients in p starting from a measured interferogram. We use three examples with increasing complexity to explain the algorithm subtleties. Section 3 contains a discussion on the robustness and possible systematic errors in the nonlinearity characterization. Section 4 introduces new metrics for the strength of nonlinearity in an interferogram. Section 5 describes how the individual measurement nonlinearity characterizations can be used to correct a time series of measurements and how this may affect the atmospheric gas retrievals derived from them. Examples for all three networks are presented: ozone retrievals for an NDACC site and DMF retrievals with the COCCON and TCCON retrieval algorithm for several sites. We discuss the similarities and differences between the proposed method and the standardized TCCON nonlinearity correction approach.

Throughout this paper, an interferogram I or a spectrum S is a sequence of numbers and standard arithmetics is assumed to be performed on each element separately (e.g. a power series of an interferogram) unless stated otherwise as for a convolution product between spectral sequences. $I[i]$ denotes the selection of a specific element at an index i (for example at the ZOPD position). Coefficients of a polynomial p acting on the true interferogram values are denoted a, b for the quadratic and cubic terms respectively. Coefficients for a nonlinearity characterization polynomial p^{-1} are denoted with a prime $a', b', \ldots$.

2 Nonlinearity characterization for a single interferogram

To explain and demonstrate the proposed nonlinearity characterization algorithm we discuss three different examples to which the method was applied, with gradually increasing complexity. Before going into the details of the algorithm, it is worthwhile to review some mathematical properties of the DFT.

2.1 Circular convolution and the phase of the autocorrelations

The complex spectrum S obtained by applying the DFT on a real-valued interferogram with N elements, has a conjugate symmetry property: complex conjugation combined with reversing the elements in the spectrum sequence (McClellan et al., 2016). In practice this allows to split the complex spectrum in two, the negative and positive frequencies parts. In figures with spectra (as in Fig. 1) we will typically only show the positive frequencies part of the full complex spectrum S. In order to explain and apply well known properties of the Fourier-transform such as the convolution theorem, the N-point spectrum S must be periodically continued to an infinite series of points (also known as aliasing). This periodic extension is the key concept in the definition of the N-point circular convolution appearing in Eq. (2).

The first autocorrelation in Eq. (2) (the quadratic term) is illustrated in Fig. 2 for an ideal bandpass similar to Fig. 1. The sliding window (the "flipped" spectrum) is shown in front of the periodically extended spectrum S for two different positions

https://doi.org/10.5194/egusphere-2026-1890
Preprint. Discussion started: 14 April 2026

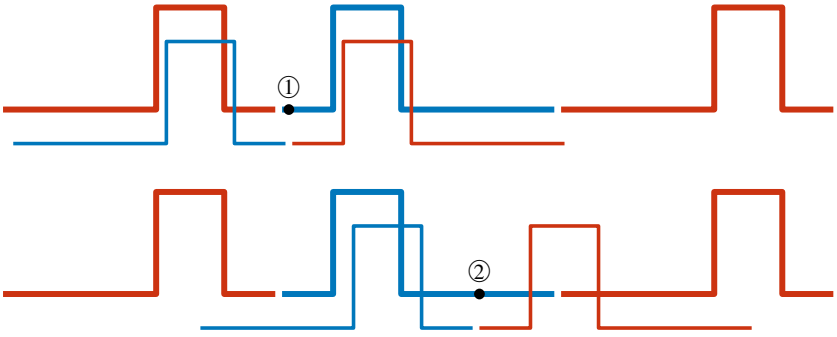

Figure 2. Autocorrelation and the circular convolution operation: the ideal bandbass from Fig. 1 is indicated in blue and corresponds to the positive frequencies part of a spectrum S obtained from the real-to-complex DFT. The negative frequencies part (red) is the complex conjugated "mirror" of the positive frequencies part and they are aliased to construct the periodically extended spectrum. The sliding window consists of a flipped copy of the neg. and pos. frequency components in S. The convolution is shown for two positions in the positive frequency range: (1) is located on the left of the in-band region and will have vanishing complex phase (the sliding window only pairs points from the pos. and neg. frequency parts) while (2) is located on the right and will have a doubled complex phase (non-zero pairing is done between pos. frequency parts).

(1) and (2). The circular convolution operation acts similar to the well-known standard numerical convolution operation where the sliding window is moved from the left to the right, at each position summing the point-wise product of the periodically extended spectrum with the finite convolution window. In Fig. 2 the positive and negative frequencies part of S are shown with distinct colors to indicate how complex numbers in S are paired by multiplication in the convolution operation. The first position (1) corresponds to a value of the autocorrelation for a position on the left side of the in-band region and has zero phase since all complex values from the periodically extended complex spectrum S are multiplied with their complex conjugates in the sliding window (the flipped spectrum). The second position corresponds to an autocorrelation value on the right side of the in-band region where the phase of the positive frequencies are doubled.

This demonstrates the phase jumps in the quadratic autocorrelation in the idealized example in Fig. 1(b), going from zero on the left of the in-band region to twice the in-band phase on the right of the in-band region. This phase behavior is inherently part of the convolution operator in right hand side of Eq. (2) and should therefore also be present in the nonlinearity induced quadratic artifact in the out-of-band region of the measured spectrum. A similar conclusion holds for the phase of higher order autocorrelations.

Being a standard operation in FTIR processing, phase correction is normally applied to obtain a real spectrum from the generally complex S returned by the DFT so that it can be used in the atmospheric gas retrievals (Mertz, 1967; Forman et al., 1966; Herres and Gronholz, 1984). We found that the out-of-band phase information plays a crucial role to disentangle cubic from quadratic nonlinearity artifacts and to separate nonlinearity artifacts from other out-of-band spectral features (Messerschmidt et al., 2010; Dohe et al., 2013). Phase correction is therefore not applied on the complex spectrum obtained from the DFT in the proposed algorithm. The FTIR standard operations are applied to the nonlinearity corrected interferograms only. Throughout

https://doi.org/10.5194/egusphere-2026-1890
Preprint. Discussion started: 14 April 2026

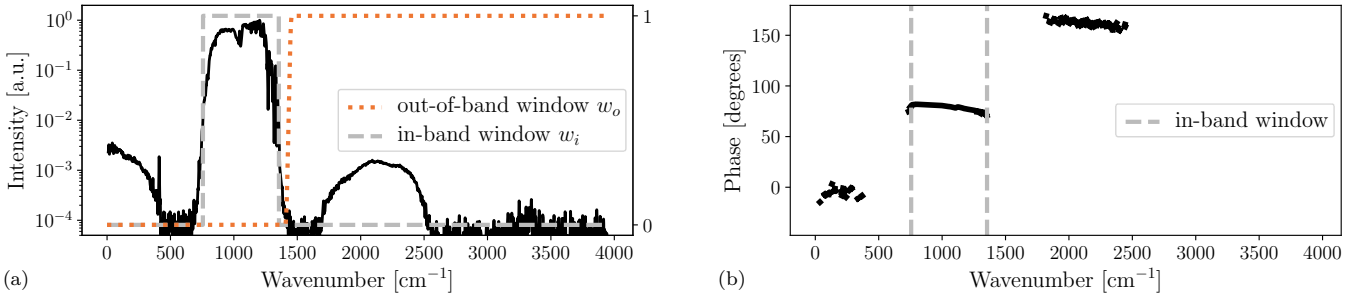

Figure 3. An MCT spectrum recorded at the NDACC Maïdo observatory on Dec 9 2019. (a) The amplitude spectrum $|S^e_m|$ of the envelope on a logarithmic scale along with the out-of-band window w_o used to fit the nonlinearity artifacts and in-band window w_i used to estimate S_t. (b) The phase values of the complex spectrum S^e_m in the regions where the spectrum has a signal. The filter window is chosen such that it contains the intensities above 1% of the amplitude spectrum maximal intensity (normalized at 1). Spectral artifacts appear around 250 cm $^{-1}$ and 2100 cm^{-1}.

this paper the visualization of the positive frequency component of a spectrum S is done similar to Fig. 1 where the *amplitude spectrum*, the real valued spectrum obtained by taking the modulus of the individual complex numbers in S and denoted with $|S|$ (Herres and Gronholz, 1984), is shown in the left panel and the phase of S in the right panel.

2.2 Example 1: a narrowband spectrum from an NDACC MCT AC-coupled interferogram

The first example shown in Fig. 3 has a quadratic spectral out-of-band artifact seen in both lower and higher wavenumbers compared to the in-band region centered at 1150 cm^{-1}. The phase of the in-band spectrum has a similar linear wavenumber dependence as in the ideal bandpass example in Fig. 1 from the introduction. This particular example was chosen because it allows to explain the basics of the algorithm and to demonstrate how the phase of the complex measured spectrum is used to estimate the quadratic coefficient in p in the absence of cubic artifacts.

The complex spectrum in Fig. 3 is obtained from the measured AC interferogram by selecting a symmetric region around the center burst with a radius (arm length) of $2^{11} = 2048$ points as shown in Fig. 4. This truncated double sided interferogram I^e_m is less affected by measurement noise and determines the envelope of the spectrum obtained from the full interferogram. The superscript e refers to this envelope property. Note that a similar truncation towards a double sided interferogram is also used for the estimation of the phase in the Mertz phase correction (Mertz, 1967). To eliminate as much as possible the measurement noise in the out-of-band region, the interferogram I^e_m is apodized with the three term Blackmann-Harris window (B_3) (Harris, 1978; Herres and Gronholz, 1984). Eq. (1) remains valid for I^e_m since it acts on the individual elements in the interferogram and I^e_m is simply a truncated double sided portion of I_m. Both sides of Eq. (2) should be convoluted with the DFT of the chosen apodization. The next step is to choose an appropriate filter window w_i in the spectral domain as in Fig. 3(a) that extracts the in-band spectrum and filters the out-of-band artifacts $S^e_{m,i} = w_i S^e_m$. Typically w_i is a box window whose cutoff wavenumbers coincide with the cut on and cut off of the bandpass of the optical filter used in the instrument.

https://doi.org/10.5194/egusphere-2026-1890
Preprint. Discussion started: 14 April 2026

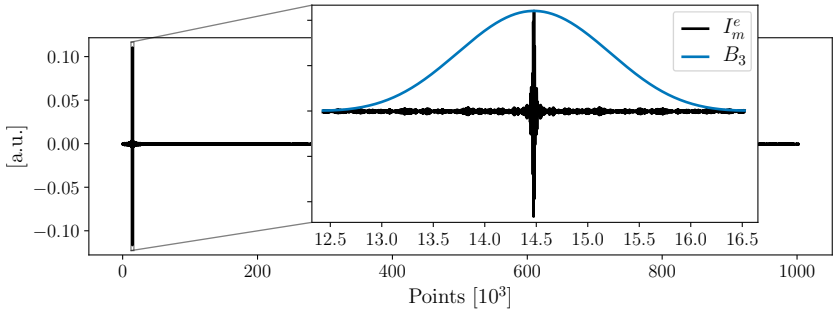

Figure 4. A truncated double sided interferogram I_m^e is extracted from the full interferogram where each side has 2048 points. The chosen apodization function B_3 is indicated in blue and is multiplied with I_m^e before applying the DFT.

Following Knuteson et al. (2004), the true spectrum in the right-hand side of Eq. (2) is replaced with the in-band filtered measured spectrum $S_{m,i}^e = w_i S_m^e$. The higher order autocorrelations of the true spectrum in Eq. (2) are in turn approximated by $S_{m,i}^{e,2} = (S_{m,i}^e \otimes_N S_{m,i}^e)$ and $S_{m,i}^{e,3} = (S_{m,i}^{e,2} \otimes_N S_{m,i}^e)$ (and similar for even higher order terms). The relation in Eq. (2) then simplifies to an equation where only the coefficients $a, b, \ldots$ of p are unknown:

$$S_m^e = S_{m,i}^e + aS_{m,i}^{e,2} + bS_{m,i}^{e,3} + \cdots . \tag{3}$$

We discuss the validity of these approximations in Sect. 3. For now we can assume that the coefficients from Eq. (2) are also valid for the relation in Eq. (3).

Going back to the example in Fig. 3 with a chosen in-band window, the autocorrelations $S_{m,i}^{e,k}$ of order $k = 2, \ldots$ can be calculated and verified if they are in the out-of-band region. In this example only the second order autocorrelation $S_{m,i}^{e,2}$ appears in the out-of-band region. An out-of-band window w_o is selected such that it contains the second order autocorrelation term. This out-of-band window w_o should be complementary to the in-band window with $w_o w_i = 0$: when multiplying both sides of Eq. (3) with w_o and assuming $b = 0$, we get a simplified equation

$$w_o S_m^e = a w_o S_{m,i}^{e,2}. \tag{4}$$

The real and complex part of the measured spectrum in the left-hand side of Eq. (4) is shown in Fig. 5(a). Using the phase ϕ_2 of the quadratic complex sequence $S_{m,i}^{e,2}$, we rotate both sides of Eq. (4) towards the phase of the quadratic term. A least square (LSQ) fit is then applied on the real part of the rotated terms in this equation:

$$\min_{a\in\Re} \left\| \Re\left(w_o e^{-i\phi_2} \left(S_m^e - aS_{m,i}^{e,2} \right) \right) \right\|^2 = \min_{a\in\Re} \left\| w_o \left(\Re\left(e^{-i\phi_2} S_m^e \right) - a \left| S_{m,i}^{e,2} \right| \right) \right\|^2 . \tag{5}$$

From Fig. 5(b), the autocorrelation term $aw_o|S_{m,i}^{e,2}|$ fits nicely with the shape of the rotated measured spectrum. The rotated measured out-of-band spectrum has a nearly vanishing complex part, suggesting the observed spectral artifact is entirely due to the quadratic nonlinearity. The uncertainty on the fitted coefficient a can be estimated using the noise in the spectrum and should be used to evaluate the quality of the fit. This is discussed in more detail in Sect. 3.

https://doi.org/10.5194/egusphere-2026-1890
Preprint. Discussion started: 14 April 2026

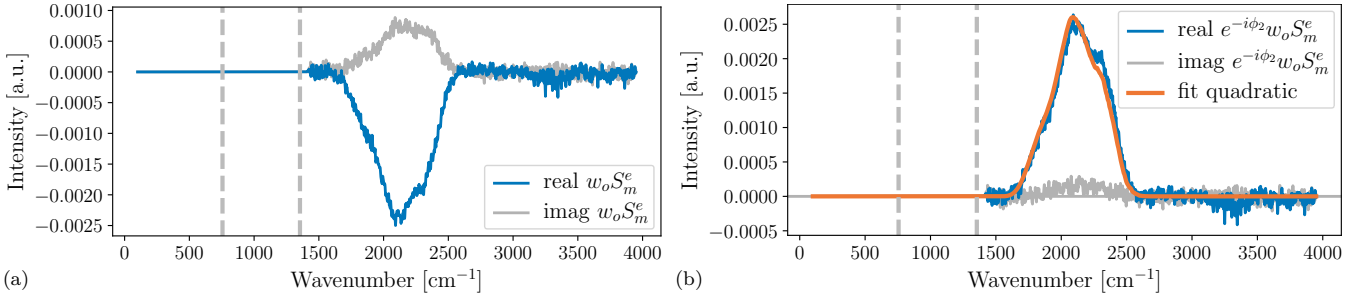

Figure 5. (a) The measured complex spectrum array S^e_m filtered to the selected out-of-band window w_o. (b) The same array but rotated with the opposite phase $-\phi_2$ of the quadratic autocorrelation term $S^{e,2}_{m,i}$. The real component of the rotated spectrum allows an LSQ fit (in orange) on the quadratic coefficient a that scales $S^{e,2}_{m,i}$. Vertical lines indicate the boundaries of the chosen in-band window.

The nonlinearity correction itself becomes a straightforward step once the quadratic coefficient a is determined. The inverse series $p^{-1}(x) = 1 + a'x + b'x^2 + \cdots$ for $p(x) = 1 + ax$ has coefficients $a' = -a$, $b' = 2a^2$, $c' = -5a^3, \ldots$ (Morse and Feshbach, 1953; Weisstein, 2026) and is applied to the original AC interferogram (we truncate the infinite series expression for p^{-1} at order 6). The baseline of the resulting corrected spectrum has reduced out-of-band artifacts, see Fig. 6. Note that the in-band spectrum is unchanged because there is no cubic artifact in this particular example.

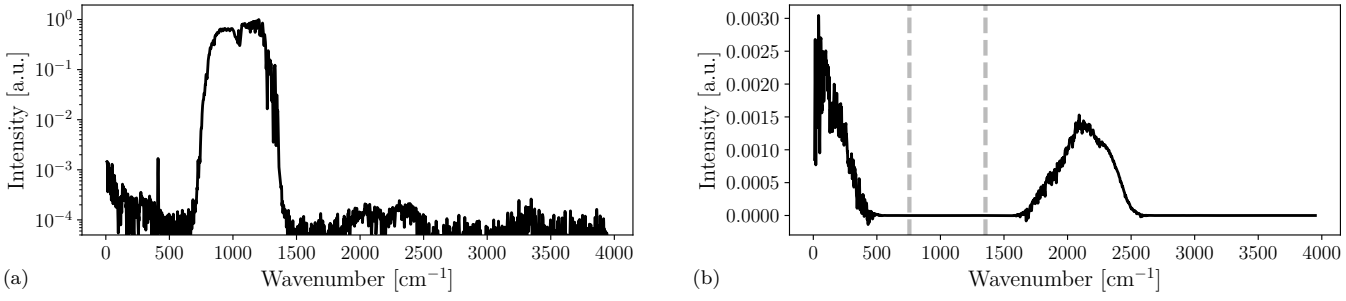

Figure 6. (a) The corrected amplitude spectrum with $a = 0.044$. (b) Amplitude spectrum of the difference between the two envelope spectra (original minus corrected). Because the bandwidth is narrow enough, the in-band region remains unchanged. Vertical lines indicate the boundaries of the chosen in-band window.

2.3 Example 2: a narrowband spectrum from an InGaAs DC-coupled interferogram

This example is chosen to demonstrate that a nonlinearity characterization requires a careful selection of the out-of-band window w_o to avoid other spectral artifacts. The additional complexity for nonlinearity characterization of DC recorded interferograms is also introduced. A narrowband InGaAs measurement setup is used in the TCCON/COCCON networks to characterize ghosts in the spectral domain. Similarly to nonlinearity artifacts, ghosts are spectral artifacts that can also be observed in the out-of-band region but are caused by an instrument laser sampling error (Messerschmidt et al., 2010; Dohe et al., 2013). The

https://doi.org/10.5194/egusphere-2026-1890
Preprint. Discussion started: 14 April 2026

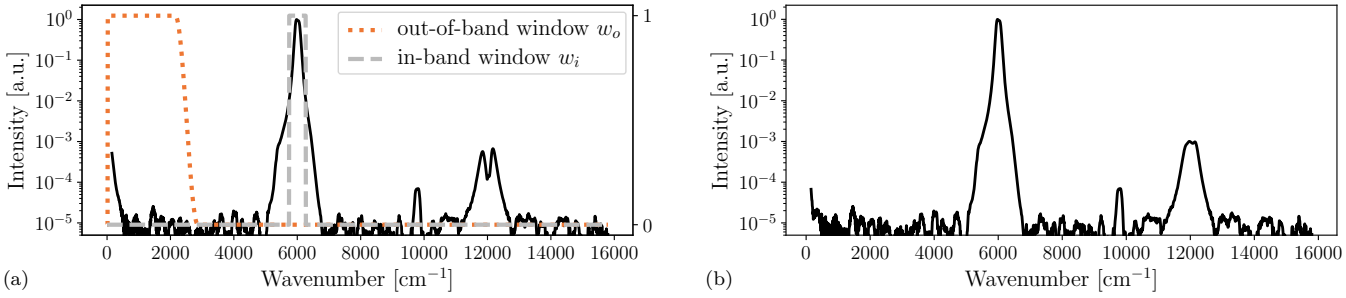

Figure 7. (a) The amplitude spectrum of the envelope of a low-spectral resolution measurement obtained with a Bruker Invenio-R instrument in order to determine the ghost-to-parent intensity ratio. The spectral artifact at 12000 cm^{-1} is a combination of an internal reflection and the quadratic nonlinearity artifact. (b) The amplitude spectrum of the envelope of the nonlinearity corrected measurement, the dip on top of the spectral artifact at 12000 cm^{-1} is removed.

optical filter (Spectrogon NB-1670-048) used in the spectrum in Fig. 7 has a central frequency at 5988 cm$^{-}1$ and the spectrum has a ghost feature at 9810 cm^{-1}. There is an additional spectral artifact at twice the narrowband wavenumber 12000 cm^{-1} which is not completely understood and assumed to be caused by an instrument internal reflection. This unknown feature turns out to overlap with the quadratic nonlinearity artifact. To distinguish DC from AC interferogram characterizations, DC is indicated in super- or subscript wherever relevant, e.g. I_m^{DC}.

Similarly to the previous example, the first step is to extract a double sided AC interferogram I_m^e out of the DC recorded interferogram I_m^{DC}. This can be done by subtracting the scalar DC level d_c at the center burst from the truncated DC interferogram (again using a radius of 2048 points). The DC level is estimated by fitting a line through the tails of the truncated DC interferogram and d_c is the interpolated value at the center burst position. The methodology described in the first example can then be applied on the AC envelope interferogram to estimate the polynomial coefficients for p and consequently for the inverted power series p^{-1}. The autocorrelations derived from the AC in-band envelope spectrum are shown in Fig. 8. The in-band window bounds are defined using a 1% threshold on the envelope amplitude spectrum (see Fig. 7 (a) and Sec. 3 for a more detailed discussion on the choice of the threshold). Similarly to the previous example, the cubic autocorrelation does not match a measured artifact and can be ignored ($b \approx 0$). From Fig. 8(b) we see that the phase of the quadratic autocorrelation coincides with the measurement out-of-band phase for the wavenumbers close to zero while it does not match the phase at 12000 cm^{-1}. The quadratic artifact on the right of the filter window should therefore be discarded and left out from the out-of-band window w_o.

The corresponding polynomial p_{DC}^{-1} acting on the original DC interferogram I_m^{DC} is related to p^{-1} by means of a scalar shift: $p_{\mathrm{DC}}^{-1}(I_m^{\mathrm{DC}}) = p^{-1}(I_m^{\mathrm{DC}} - d_c)$ (Lachance, 2000). The shifted polynomial has a non zero scalar term and a linear coefficient different from 1. For our purposes the absolute interferogram values are not required and we can remove the scalar term and scale the polynomial so that it again takes the form $p_{\mathrm{DC}}^{-1}(x) = x + a'x^2 + \cdots$. The nonlinearity corrected spectrum in Fig. 7(b) is obtained from the interferogram $p_{\mathrm{DC}}^{-1}(I_m^{\mathrm{DC}})$.

https://doi.org/10.5194/egusphere-2026-1890
Preprint. Discussion started: 14 April 2026

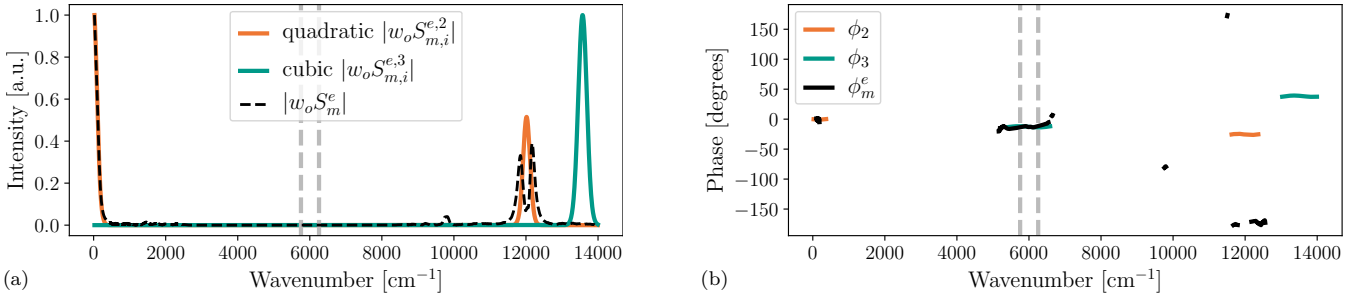

Figure 8. (a) The amplitude spectra in the out-of-band region of the measured spectrum and the higher order autocorrelation terms, all scaled to have their maximum amplitude equal to 1. The quadratic term coincides with the measurement out-of-band artifact at wavenumbers below 1000 cm^{-1} but deviates at 12000 cm^{-1}. The cubic term does not overlap with a measured artifact. (b) Phase sequences restricted to the regions where there is a signal, ϕ^e_m denotes the phase of S^e_m. At 12000 cm^{-1} the phase of the quadratic term $\phi_2[12000\ \text{cm}^{-1}] \approx -20°$ does not match the phase of the measurement $\phi^e_m \approx -170°$ (i.e. they are not equal nor opposite).

2.4 Example 3: a TCCON spectrum from an InGaAs DC-coupled interferogram

Compared to the previous narrowband examples, the standard operations spectra recorded in the TCCON or COCCON are more challenging for nonlinearity characterization because the autocorrelations overlap in the narrow out-of-band region. We present two examples: one spectrum recorded at the Saint-Denis (Réunion Island, France) TCCON site (De Mazière et al., 2022) and one at the Sodankylä (Finland) TCCON site (Kivi et al., 2022). Both measurements allow to show how the algorithm can be applied to estimate higher order coefficients in p (up to the cubic coefficient). Although both quadratic and cubic autocorrelations overlap with each other in the out-of-band region, it remains possible to disentangle the cubic from the quadratic term by making use of their complex phase (Sodankylä example) and by making a dedicated choice of out-of-band windows for each nonlinearity term separately (Saint-Denis). Figure 9 shows the original and nonlinearity corrected spectra at Saint-Denis while Fig. 10 shows the autocorrelations of the in-band spectrum. The LSQ fit to find coefficients a, b from Eq. (3) is applied to a concatenation of two real sequences (one for each coefficient) obtained by rotating Eq. (3) with $-\phi_2$ and $-\phi_3$

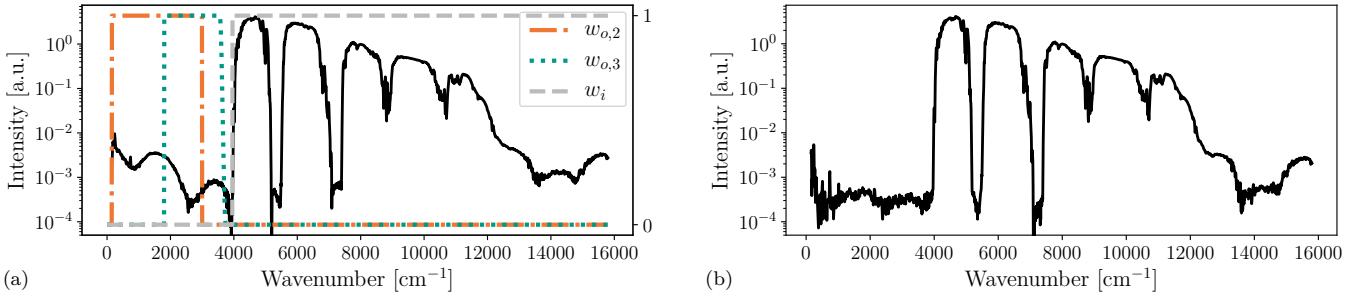

Figure 9. (a) The amplitude spectrum of the envelope of a standard TCCON measurement obtained with a Bruker IFS 125HR instrument at Saint-Denis (Réunion Island) (b) The envelope of the nonlinearity corrected measurement.

https://doi.org/10.5194/egusphere-2026-1890
Preprint. Discussion started: 14 April 2026

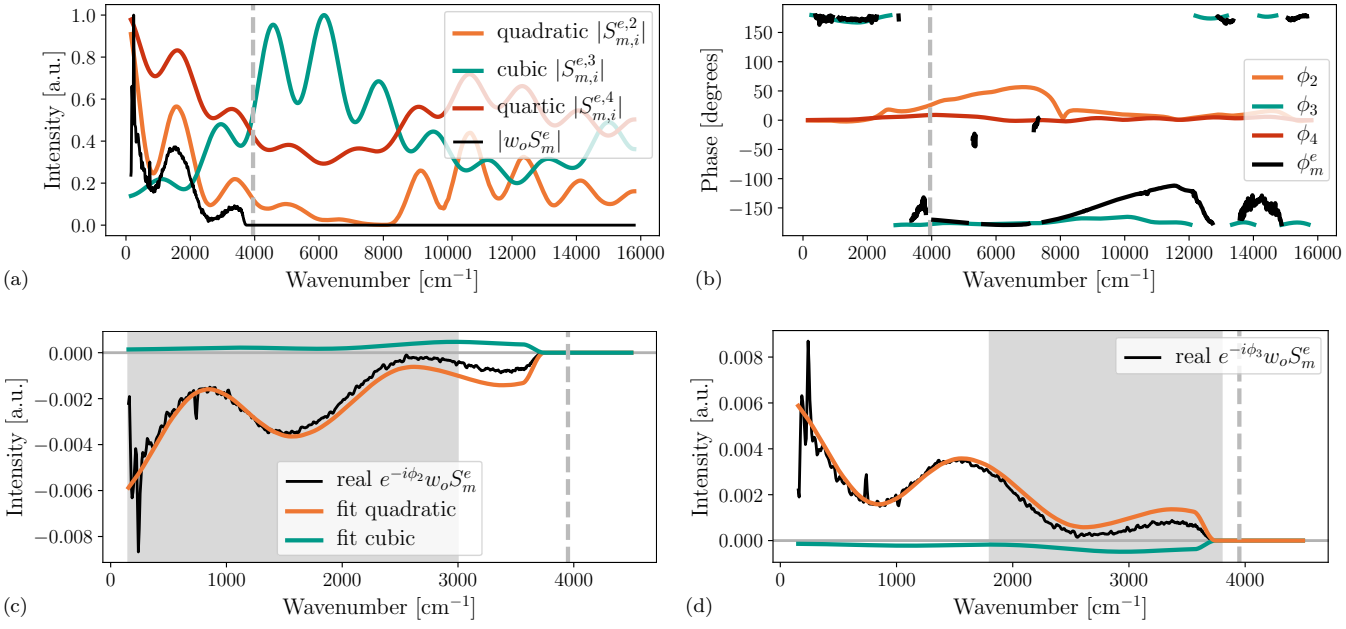

Figure 10. (a) The amplitude spectra for the out-of-band measured spectrum and the higher order autocorrelation terms, all normalized to have maximal amplitude equal to 1. Quadratic and cubic artifacts overlap in the out-of-band region. (b) Phase arrays. Quadratic and cubic terms have opposite phase in the out-of-band region. ϕ^e_m denotes the phase of S^e_m. (c) The real component of the $-\phi_2$ complex rotated measurement, quadratic and cubic terms. The shaded area indicates the out-of-band window $w_{o,2}$. (d) Similar as (c), but rotated with $-\phi_3$ and showing $w_{o,3}$.

respectively. Each sequence is restricted to a dedicated subwindow of the out-of-band window, denoted $w_{o,2}$ and $w_{o,3}$, that captures the relevant autocorrelation:

$$\min_{a,b\in\Re} \left(\left\| \Re\left(w_{o,2} e^{-i\phi_2} \left(S^e_m - a S^{e,2}_{m,i} - b S^{e,3}_{m,i} \right) \right) \right\|^2 + \left\| \Re\left(w_{o,3} e^{-i\phi_3} \left(S^e_m - a S^{e,2}_{m,i} - b S^{e,3}_{m,i} \right) \right) \right\|^2 \right) . \tag{6}$$

Figures 10(c) and (d) show the two concatenated components used in the LSQ fitting defined in Eq. (6) separately. The quadratic fit does not match well with the measurement between 2000 and 3000 cm^{-1}: this is caused by the cubic nonlinearity where it reaches its highest value in the out-of-band window, see Fig. 10(a). For that reason we have defined $w_{o,3}$ to coincide with the region where cubic nonlinearity is strongest. The window $w_{o,2}$ is wider and coincides with the lower wavenumber where the quadratic feature is more prominent. It only partly overlaps with $w_{o,3}$ which should guarantee a less correlated fit of the two coefficients a, b. Some overlap is kept for a better quadratic fit in case the cubic artifact is weak and not present. This example is special in the sense that the quadratic and cubic phases are close to being opposite ($\approx 0°$ and $180°$) and both rotated sequences in the quadratic $w_{o,2}$ and cubic $w_{o,3}$ windows are in the same complex plane. This is not the case for the Sodankylä example in Fig. 11. With the same in- and out-of-band windows, the cubic autocorrelation has a phase nearly perpendicular to the quadratic autocorrelation and the two fit windows provide a different view on the measured out-of-band feature.

https://doi.org/10.5194/egusphere-2026-1890
Preprint. Discussion started: 14 April 2026

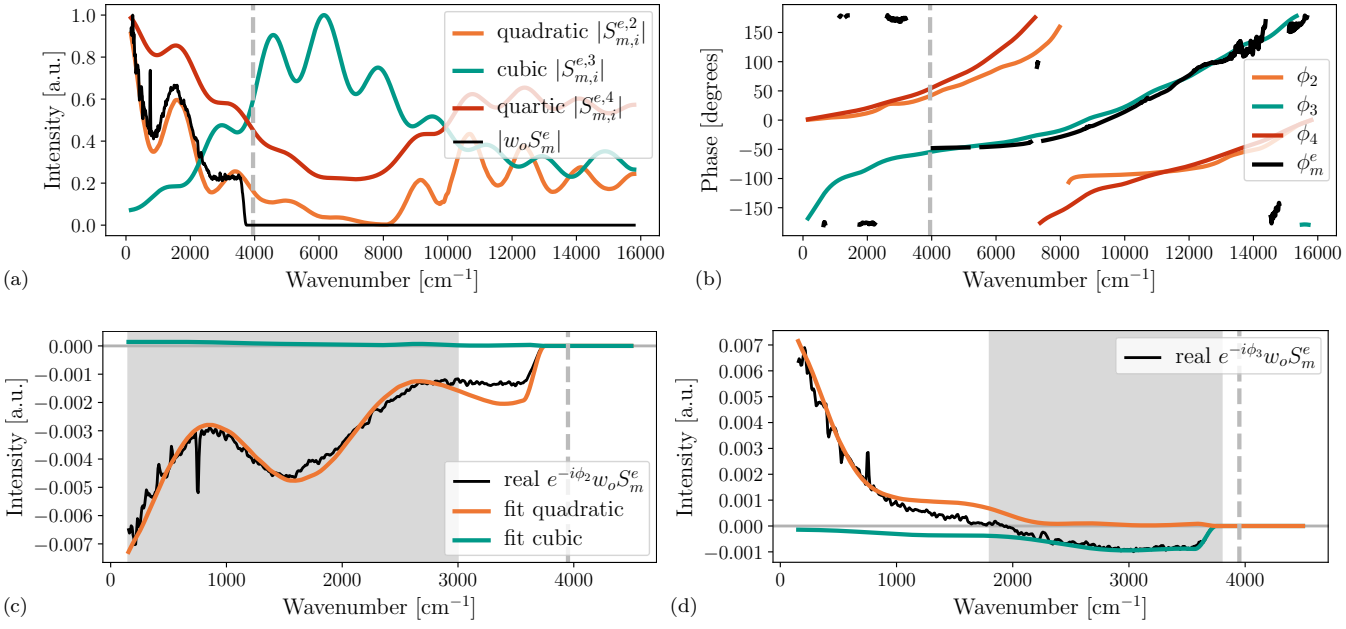

Figure 11. Similar to Fig. 10 but for a measurement obtained with a Bruker IFS 125HR instrument at Sodankylä (Finland). The quadratic and cubic phase are nearly perpendicular in this case.

The cubic nonlinearity feature is much less prominent in the out-of-band region compared to the quadratic and this is reflected in the associated LSQ fitting uncertainties where the cubic uncertainty is two to four times higher when compared to the uncertainty of the quadratic coefficient estimate. A more detailed discussion on the estimate uncertainty is postponed to Sect. 3.

2.5 Algorithm summary

The algorithm presented above is summarized by the following steps and schematized in Fig. 12.

1. Extract a double sided interferogram I^e_m around the center burst; in the case of a DC recorded interferogram, substract the DC level d_c.
2. Apply the DFT on I^e_m to go to the spectral domain; select an in-band window and calculate the autocorrelations of $w_i S^e_m$ for orders $2, 3, \ldots$
3. Select the out-of-band windows $w_{o,k}$ for each order k such that the autocorrelation $S^{e,k}_{m,i}$ coincides both in amplitude and phase with a spectral artifact in the measured spectrum; use a LSQ in these subwindows fit to estimate the coefficients of p.
4. Use the reverse power series formula from Weisstein (2026) to calculate the coefficients for p^{-1} from the estimated coefficients $a, b, \ldots$ of p.

https://doi.org/10.5194/egusphere-2026-1890
Preprint. Discussion started: 14 April 2026

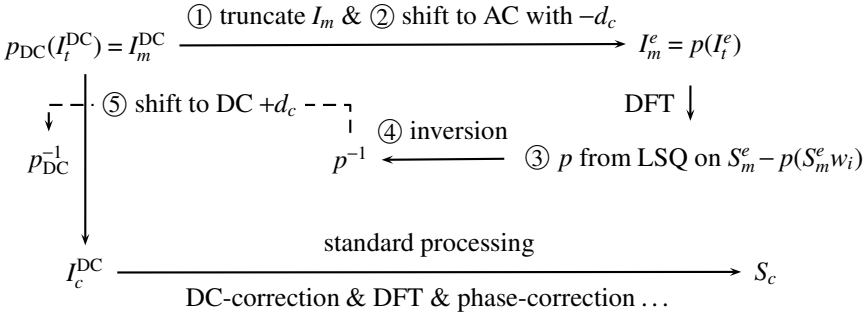

Figure 12. Diagram representing the steps required to obtain a nonlinearity characterization p_{DC}^{-1} (up to step 5) for a single interferogram I_m^{DC} and a nonlinearity corrected interferogram I_c^{DC} . The final step leading to a nonlinearity corrected spectrum is then obtained using the network's (TCCON, COCCON, NDACC) standard processing algorithm which includes a DC-correction (to reduce the impact of source brightness fluctuations), the application of apodizations, the DFT and a phase correction.

5. In the case of a DC recording, calculate the coefficients of the shifted polynomial $p_{DC}^{-1}(x) = p^{-1}(x - d_c)$ with the DC level d_c from step 1 .

The choice of the in-band window can be largely automated: a default in-band window can be derived from the amplitude spectrum $|S_m^e|$ as the wavenumber range that contains the higher intensities (a threshold of 1% of the maximum intensity is used in the examples). The third step, estimating the coefficients of p, involves choosing appropriate out-of-band window(s) and requires a visual check on the autocorrelations and the measurement out-of-band features. The choice of these subwindows depends on the instrument setup: filter window, presence of other spectral artifacts such as internal reflections or ghosts, or interferogram undersampling (see below). The subwindow selection neither depends on the chosen maximum optical path difference nor on the instrument aperture setting. It should be done only once for each filter window in an instrument setup. In practice this means that the same subwindow selection can be used for all measurements in the TCCON and COCCON.

For MCT and InSb measurements taken in the framework of the NDACC (narrow-band setup in the lower wavenumber range), the out-of-band window is typically chosen to coincide with wavenumbers larger than the in-band window upper bound, while for InGaAs measurements as in COCCON or TCCON the out-of-band window is chosen by default to coincide with the wavenumbers below the detector response cut-off wavenumber at 4000 cm^{-1}.

The LSQ fit in step 3 uses the Levenberg-Marquardt minimization algorithm as implemented in SciPy (Virtanen et al., 2020; Moré, 1978) where the cost function is weighted with a vector representing the noise in the out-of-band windows (higher noise corresponds to lower weights). The algorithm gives an uncertainty estimate on the returned coefficients. Estimates with high uncertainty should be rejected: for example, if the cubic nonlinearity in a spectrum is very weak and comparable to the noise in the out-of-band region, its uncertainty will be higher and the estimated cubic coefficient b should be considered unreliable. Appropriate thresholds for the uncertainties can be derived from a sample of interferograms: in the TCCON and COCCON examples in Sect. 5 the thresholds used are 1.5% and 6% for the quadratic and cubic coefficients respectively. The algorithm takes these estimate uncertainties and thresholds into account in an iterative way. Starting with a simultaneous fit

https://doi.org/10.5194/egusphere-2026-1890
Preprint. Discussion started: 14 April 2026

of the quadratic and cubic coefficients (as in the third example), the fit uncertainties for a and b may not exceed the given thresholds. If one of uncertainties is considered too high, the LSQ fit is re-run but only fitting the quadratic coefficient. If the fit uncertainty for a remains above the 1.5% threshold, the algorithm fails and no reliable nonlinearity characterization was possible. This typically occurs when the detector response was not affected by nonlinearity or when the signal in the spectra is weak (too high noise levels).

Due to the narrow-band setup in the NDACC, interferograms are often recorded with a high (or low) folding limit (Herres and Gronholz, 1984). The algorithm can be applied to such undersampled interferograms as long as the out-of-band is sufficiently large to capture the autocorrelations (undersampling was done in the first MCT example). Different settings for interferogram undersampling might therefore affect the subwindow selection in step 3.

The extension of the algorithm to estimate the higher order coefficients $c, d \ldots$ in p is straightforward: for a given maximal degree n for the polynomial p and out-of-band subwindows $w_{o,k}$, $k = 2, \ldots, n$, the cost function for the LSQ takes the more general form

$$\sum_{k=2}^{n} \left\| \Re\left(w_{o,k} e^{-i\phi_k} \left(S^e_m - p(S^e_{m,i}) \right) \right) \right\|^2 . \tag{7}$$

We have encountered few examples where we could confidently estimate higher order features (above cubic) in the out-of-band signal (see Sec. 5.1).

3 Algorithm sensitivities and applicability

The LSQ uncertainty estimates for the fitted coefficients a, b should be taken into account to discard unreliable fits from too noisy spectra. In addition, a discussion of possible systematic errors in the proposed algorithm is necessary. We consider three different sensitivity tests. The first verifies the key assumption in the algorithm that the true spectrum can be approximated by the in-band measured spectrum. The second test perturbs the in-band window boundaries. The third test checks the sensitivity to the chosen apodization.

3.1 Approximation of the true spectrum with the in-band measured spectrum

Recall that the validity of Eq. (3) relies on the assumption that the in-band measured spectrum $S^e_{m,i}$ approximates the true spectrum. But in the presence of nonlinearity artifacts, the measured spectrum may deviate from the true spectrum also in the in-band region: $S^e_{m,i} = w_i(S_t + aS_t \otimes_N S_t + \cdots)$. The autocorrelations $S^{e,2}_{m,i}$, $S^{e,3}_{m,i}$ calculated as part of the algorithm will therefore in turn deviate from the true autocorrelations and create an error on the fitted coefficients a, b. To study this error in more detail, we take an ideal shortpass filter with a similar transmission range as the InGaAs detector in example 2.4 and perturb it in-band by adding a known nonlinearity. The effect on $S^{e,2}_{m,i}$, $S^{e,3}_{m,i}$ is shown in Fig. 13 where a quadratic nonlinearity (top row) or a cubic nonlinearity (bottom row) is added to the ideal bandpass. Adding a quadratic nonlinearity term affects the phase of the cubic autocorrelation $S^{e,3}_{m,i}$ (panel (b)). Alternatively, when adding a cubic nonlinearity term the magnitude of the quadratic autocorrelation $S^{e,2}_{m,i}$ is perturbed (panel (c)). Both perturbations will cause an error on the fitted coefficients a and b

https://doi.org/10.5194/egusphere-2026-1890
Preprint. Discussion started: 14 April 2026

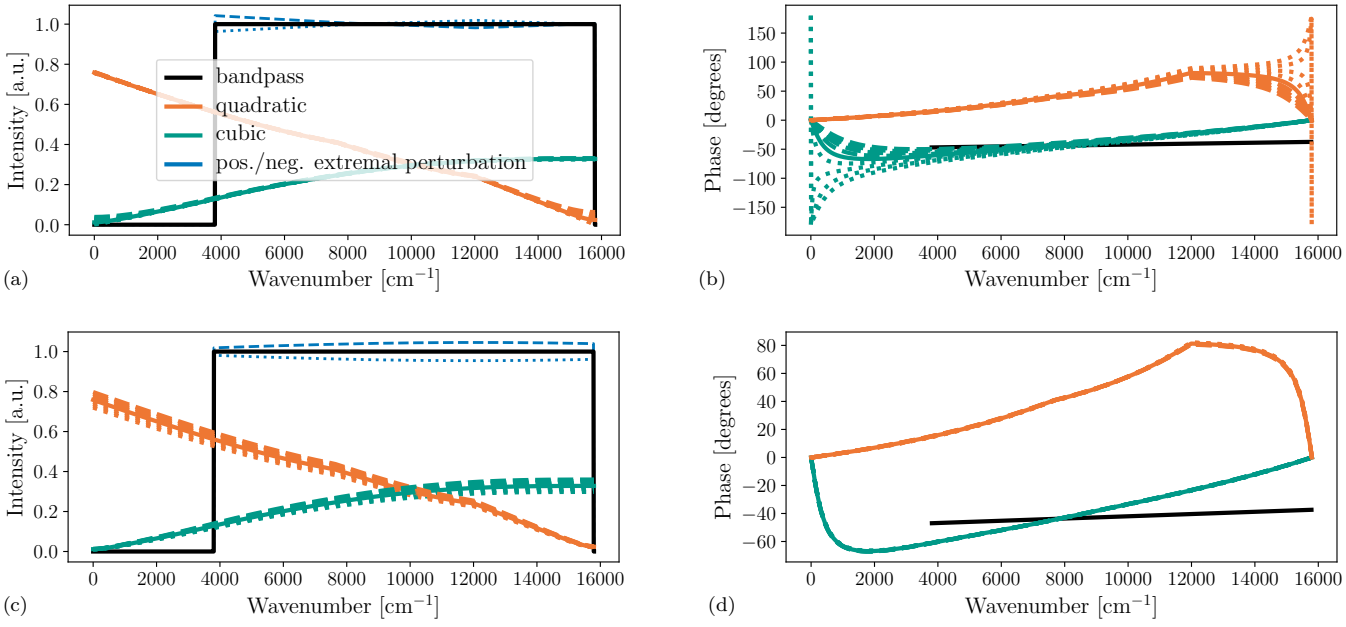

Figure 13. Autocorrelations for a nonlinearity affected idealized wide bandpass calculated from $S^e_{m,i} = w_i(S_t + aS_t \otimes_N S_t)$ (top row) and $S^e_{m,i} = w_i(S_t + bS_t \otimes_N S_t \otimes_N S_t)$ (bottom row). (a) Magnitude of autocorrelations for $S^e_{m,i}$ with $a \in [-0.01, 0.01]$. The maximally perturbed bandpass $S^e_{m,i}$ is indicated in blue ($a = \pm 0.01$). (b) Phase values of the autocorrelations in (a); dashed lines corresponds to perturbations with $a > 0$, dotted lines to $a < 0$. (c) and (d) Similar as (a), (b) but with imposed cubic nonlinearity $b \in [-0.01, 0.01]$.

which is found to be proportional but opposite in sign. The bounds on a, b for the in-band perturbations are chosen to be ± 0.01 which is large enough to contain the typical values seen in the TCCON Saint-Denis timeseries in Sect. 5. Adding a combined nonlinearity of $a = b = \pm 0.01$ causes an error of $\mp 0.8\%$ on the fitted quadratic coefficient a and of $\mp 1.1\%$ on the cubic coefficient b. A possible improvement of the proposed algorithm lies in a correction to $S^e_{m,i}$ by pre-fitting the autocorrelations and removing them from $S^e_{m,i}$. This however was found to bring only a small improvement on the fitted coefficients and the additional computational burden was considered unnecessary.

We found examples at Saint-Denis where nonlinearity affects the out-of-band region so strongly that the cubic and quadratic autocorrelations are no longer distinguishable. Under strong nonlinearity response the algorithm fails: here the fact that the quadratic and cubic spectral features become undistinguishable takes precedence over the larger systematic errors for the estimates for a and b. For Saint-Denis such strong detector saturation was found to occur when the DC-level at the center burst exceeds a specific threshold. A more detailed description of detector behavior in such extreme conditions is not under consideration in this study. These measurements are filtered from the TCCON processing.

https://doi.org/10.5194/egusphere-2026-1890
Preprint. Discussion started: 14 April 2026

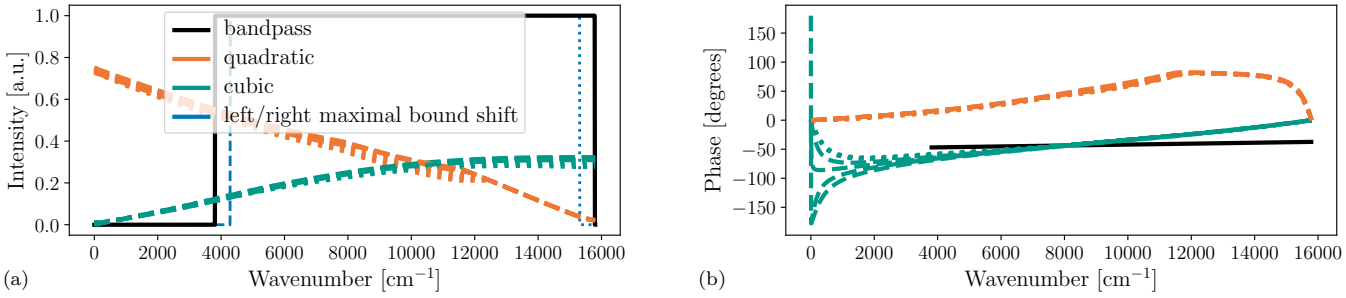

Figure 14. Autocorrelations of an idealized shortpass filter where the in-band window w_i bounds do not coincide with the filter edges, representing errors introduced by choosing too narrow boundaries for the in-band window w_i. Dashed lines corresponds to shifting the lower bound of the in-band window towards the right of the cut-off wavenumber, dotted lines correspond to shifting the upper bound towards lower wavenumbers. The blue lines show the maximal shift in lower (dashed) and upper (dotted) boundary, being 5% of the width of the ideal bandpass.

3.2 Sensitivity to the in-band window boundaries

A second sensitivity test was done on the bounds of the in-band window. Here the autocorrelations $S^{e,2}_{m,i}$, $S^{e,3}_{m,i}$ are calculated with a shifted cut-off wavenumber (shifting to the right) or by introducing a bound on the higher wavenumbers. The perturbed autocorrelations are shown in Fig. 14, varying the lower and upper boundary separately with 5% of the total bandpass width. The lower boundary perturbs the quadratic autocorrelation in the out-of-band window more strongly compared to changes in the upper boundary position. A similar effect on the phase of the cubic autocorrelations is seen: the lower boundary perturbations affects the phase more strongly. When adding a nonlinearity $a = b = 0.01$ on the ideal bandpass, the error on fitted coefficients is again proportional to the error made on the lower or upper in-band window boundaries. The quadratic coefficient is 1.5% for a positional error of 1% of the bandpass length for the lower boundary; the cubic coefficient error is 4%. In real-world examples, the effect will be smaller because the bandpass intensity is gradually increasing beyond the cut-off wavenumber due to the filter and solar radiation characteristics. This robustness check justifies the previously proposed automation for the choice of the in-band window boundaries using a threshold of 1% on the intensities in the amplitude spectrum.

3.3 Sensitivity to the chosen apodization

We have chosen the B_3 apodization function in order to reduce the noise in the spectral sequences. Other apodization functions could be used. In comparison with no apodization (i.e. a boxcar), the advantage of using a B_3 apodization lies in the reduction of the LSQ uncertainties and the reduced variability in the a, b coefficients when considering a sample of measurements. Using another apodization function does not give systematically different results for the nonlinearity characterization.

From a mathematical point of view the transition from Eq. (2) (unapodized) to (3) (apodized) is not entirely correct: a chosen apodization should be applied on the right-hand side of Eq. (2) and should therefore appear only once in the convolution products. The convolution products in Eq. (3) contain the apodization multiple times. A more correct approach would consist of

https://doi.org/10.5194/egusphere-2026-1890
Preprint. Discussion started: 14 April 2026

doing the DFT on the unapodized interferogram and convolute each autocorrelation separately with the DFT of the apodization function. We found that the error made is small (of the order of 0.1% on the estimated coefficients) and is ignored in favor of a less computationally demanding approach.

3.4 Other parameter and algorithm design choices

The number of points in the envelope spectrum is determined by the radius of the truncated interferogram (cf. step 1 of the algorithm). In the examples, the radius was chosen to be 2^{11} points (a power of 2 to benefit the Fast-Fourier Transform). Choosing a different value leads to differences of the order of 1% in the fit coefficients for the Saint-Denis example and the radius was therefore not considered an important influence parameter. Including more points reduces the LSQ fit errors but comes with a higher computational cost.

When considering higher order autocorrelations in the LSQ fit, the out-of-band windows will typically partly overlap and could have an effect in the LSQ fit. Each autocorrelation is fitted against a differently complex rotated out-of-band spectrum and, although there is an overlap in the wavenumbers, the information in the respective components of LSQ cost function is therefore not entirely identical. Given this and the limited number of independent parameters in the LSQ, partially overlapping out-of-band windows are not considered problematic.

The out-of-band windows might also have a different number of spectral points which could cause an imbalance between their associated components in the cost function of the LSQ. In the examples we considered all windows have comparable sizes. More extensive sensitivity tests on these parameters were not considered.

4 A measure for nonlinearity strength

The TCCON uses DIP height as a measure for nonlinearity (Keppel-Aleks et al., 2007). It was introduced as part of an algorithm that corrects source brightness variations in DC recorded interferograms. This correction method relies on a lowpass filter applied on the interferogram. In the presence of non-linear detector response, the lowpass filtered interferogram shows an artifact (a dip) at ZOPD related to the nonlinearity artifact in the out-of-band region. The TCCON DIP diagnostic is proportional to the height at ZOPD of this dip feature in the lowpass filtered interferogram and is used to indicate how strongly a measurement is affected by nonlinearity.

We propose an alternative method to measure the nonlinearity strength using the coefficients $a, b, \ldots$ of p. Such a measure should be invariant when an interferogram is scaled with a constant. If we multiply Eq. (1) with a constant number u, we obtain

$$uI_m = uI_t + uaI_t^2 + ubI_t^3 + \cdots = uI_t + \frac{a}{u}\left(uI_t\right)^2 + \frac{b}{u^2}\left(uI_t\right)^3 + \cdots .$$

The structure of Eq. (1) is preserved for the scaled interferogram and relates uI_m with the truth uI_t. The nonlinearity coefficients however scale with an appropriate power of $1/u$. This suggests that a scaling-invariant measure for the nonlinearity strength can be obtained by multiplying a with an interferogram property that is proportional to the scaling factor u. Such an interferogram property could be the DC-level at ZOPD (which has the disadvantage that it can only be used with DC-recorded

https://doi.org/10.5194/egusphere-2026-1890
Preprint. Discussion started: 14 April 2026

interferograms), the maximum of the envelope amplitude spectrum in the in-band region $\max\left(w_i\left|S_m^e\right|\right)$ or the peak-to-peak (PTP) of the interferogram in the center burst region $I_{\text{PTP}} = \text{PTP}\left(I_m^e\right)$. In what follows we have chosen half of the PTP-property (the peak amplitude of the interferogram) to obtain scaling-invariant coefficients $A = a(I_{\text{PTP}}/2)$ and $B = b(I_{\text{PTP}}/2)^2$. The PTP-property has the advantage that it is straightforward to calculate from an interferogram (both AC or DC recorded). Moreover, as explained below, A and B have an intuitive interpretation as a measure for the interferogram nonlinearity error (measured minus true) at the center burst.

If we take the peak amplitude $I_{\text{PTP}}/2$ as an approximation for $I_t[\text{ZOPD}]$, Eq. (1) at the center burst becomes

$$I_m[\text{ZOPD}] \approx (I_t + aI_t^2 + bI_t^3 + \cdots)[\text{ZOPD}] \approx \left(1 + \frac{aI_{\text{PTP}}}{2} + \frac{bI_{\text{PTP}}^2}{4} + \cdots\right) I_t[\text{ZOPD}]. \tag{8}$$

Each of the coefficients $A, B, \ldots$ in the right hand side can be considered a metric for nonlinearity strength: A represents the quadratic contribution to the relative error of the measured interferogram at the center burst. A similar interpretation can be given to the B coefficient: it relates to the cubic contribution to the relative error of the measured interferogram at the center burst. Given a nonlinearity characterization p, the associated values $A, B, \ldots$ will be used to indicate the strength of the nonlinearity and we call them *nonlinearity error estimates* (NLEs). They should be considered separate from each other and not summed to a total error: we have encountered examples where the quadratic and cubic NLEs are of the same order but opposite in sign (see the example in Fig. 22). Because the quadratic NLE $aI_{\text{PTP}}/2$ is typically dominant and can be estimated with higher confidence, it is used as a diagnostic nonlinearity metric for a measurement. For TCCON measurements the quadratic NLE estimate has a strong correlation with DIP (in the examples below, we found Pearson correlation coefficients above 0.9, see also Fig. 18).

5 Nonlinearity models and the impact of nonlinearity correction on atmospheric retrieval products

The impact of a nonlinearity correction on the atmospheric gas retrievals is hard to predict. The retrieval software and retrieval strategy will play an important role (microwindow selection, co-retrieved parameters such a zero-level offset, ...). In this section we present four practical examples where a nonlinearity correction is applied on a time series of measurements along with the impact on the atmospheric gas retrievals. These examples use measurement time series obtained from the three networks NDACC, TCCON and COCCON.

5.1 Nonlinearity in Bremen NDACC MCT measurements

The Bremen NDACC MCT measurements (Notholt et al., 2006) have a similar instrument setup as the example shown in Fig. 3: they use the standard optical filter for NDACC ozone measurements and are AC-recorded, similar to the example in Sect. 2.2. The nonlinearity error estimates were calculated for a sample of measurements obtained during 36 days in 2023-2025. These measurements have higher order nonlinearity errors: for the higher PTP values up to the quintic NLE could be estimated in the out-of-band region. In Fig. 15(a) the individual $A, B, \ldots$ coefficients are shown in relation to the interferogram PTP values. It reveals a dominantly linear dependence of the NLEs on I_{PTP} and that strength rapidly decreases with the order: the quartic

https://doi.org/10.5194/egusphere-2026-1890
Preprint. Discussion started: 14 April 2026

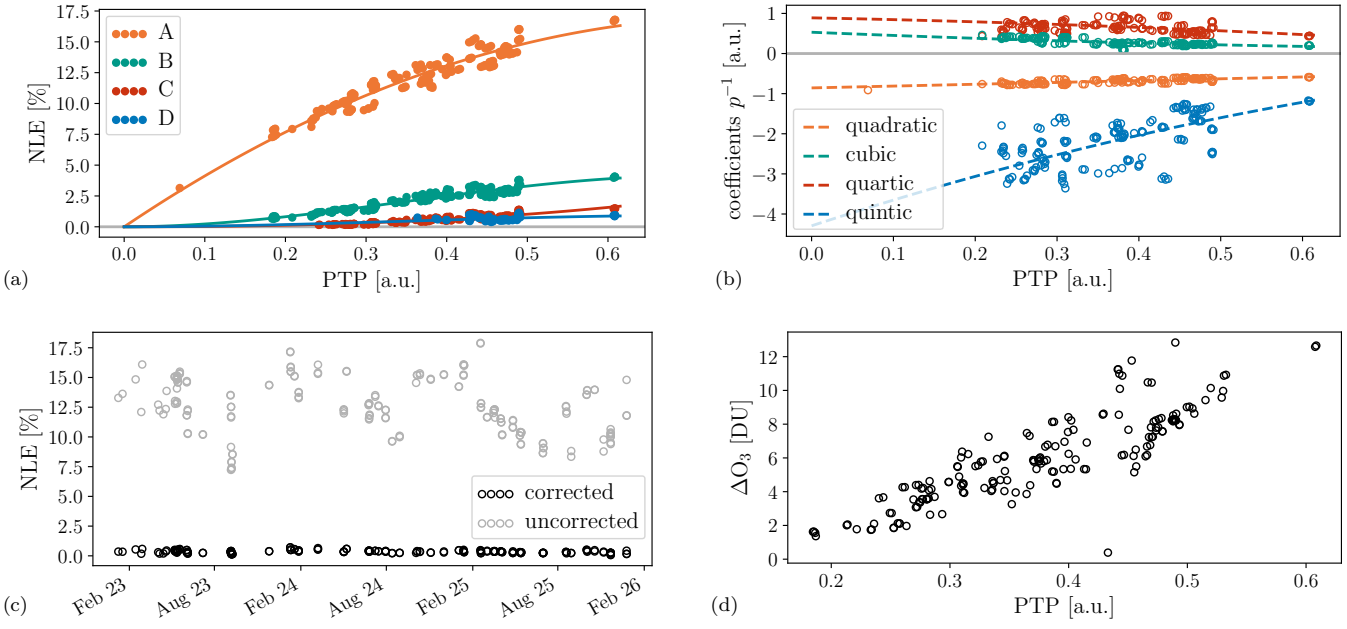

Figure 15. Nonlinearity regime for the AC-recorded NDACC MCT measurements at Bremen during 2023 - 2025 obtained from a sample of 36 days. The scale-invariant coefficients in (a) have a dominantly linear dependence on the interferogram PTP with a zero intercept. (b) The coefficients of the individual characterizations p^{-1} have a nearly constant dependence. (c) Quadratic NLE for the corrected and uncorrected measurements. (d) Difference in retrieved ozone columns (nonlinearity corrected minus uncorrected) in case the zero-level offset parameter is not co-retrieved with ozone.

and quintic NLEs are much lower compared to the quadratic and cubic NLEs reaching values of $A \approx 15\%$ and $B \approx 2\%$ for the interferograms in the sample with maximal peak amplitude. The higher order D, E are therefore not taken into account in what follows and the nonlinearity characterizations p are estimated up to third order. Panel (b) shows the quadratic, cubic, quartic and quintic coefficients of the individual nonlinearity characterizations p^{-1} (recall that the order of p^{-1} is infinite even if p is third order). Here a nearly constant dependence on the interferogram PTP is observed, only the fifth order has a slope. Panel (c) shows the timeline of the quadratic NLE values for the measured interferograms I_m and the nonlinearity corrected interferograms $I_c = p^{-1}(I_m)$ using the polynomial coefficients from panel (b).

The SFIT4 retrieval software is used to analyze these measurements (Hannigan et al., 2024). This algorithm allows to fit the zero-level of the spectral windows used for the retrieval of the atmospheric ozone profile. This co-retrieved parameter, called zshift, can capture the spectral nonlinearity error in the baseline of the retrieval windows and acts as a nonlinearity correction performed directly on the spectrum. The zshift parameter is enabled in the ACTRIS centralized ozone retrieval strategy (Vigouroux, 2025). Ozone retrievals from the original and nonlinearity corrected spectra are found to be nearly equal when zshift is fitted, with a mean difference of 0.2% which is much lower than the total uncertainty of 3.5% on the ozone columns.

https://doi.org/10.5194/egusphere-2026-1890
Preprint. Discussion started: 14 April 2026

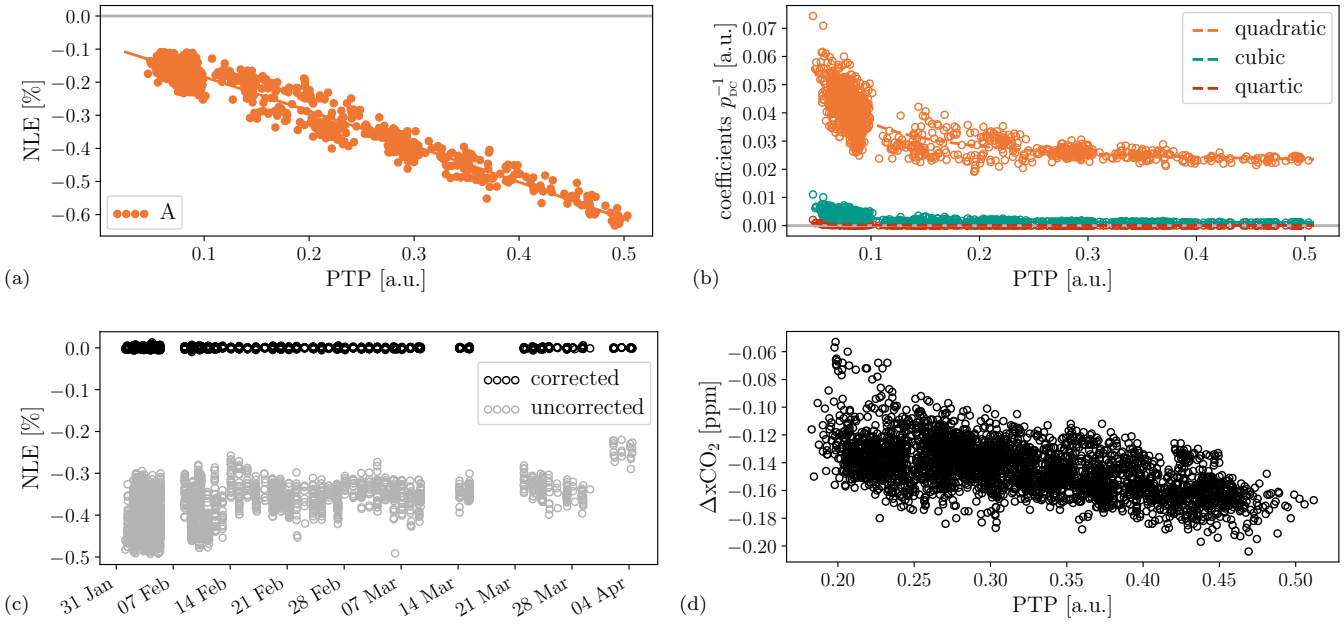

Figure 16. Similar as Fig. 15 but using the DC-recorded COCCON InGaAs measurements at Kolkata during 2023 obtained from a sample of 17 days. (d) Shows the difference in xCO_2 (nonlinearity corrected minus uncorrected DMF).

To demonstrate the importance of this zero-level parameter in the retrieval strategy and to quantify the effect of the nonlinearity correction on the ozone retrievals, the zshift parameter was disabled in the retrieval strategy. The column differences (nonlinearity corrected minus uncorrected) are shown in panel (d) in Fig. 15. The effect on the ozone columns can reach 10 DU ($\approx 2.4\%$) for the measurements with the higher PTP values.

5.2 Nonlinearity in COCCON measurements from the Vertex70 instrument at Kolkata

The InGaAs measurements obtained from the low-spectral-resolution Bruker Vertex70 instrument in Kolkata (India) have a similar setup as the TCCON InGaAs measurements but measure at a reduced spectral resolution of 0.2 cm^{-1} (maximal OPD of 4.5 cm) compared to the standard TCCON resolution of 0.02 cm^{-1} (maximal OPD of 45 cm). These DC recorded InGaAs measurements are accepted to be part of the COCCON and were therefore analyzed with the PROFFAST processor (Sha et al., 2020; Feld et al., 2024; Sha et al., 2025). During the first months in 2023 after the installation in Kolkata, the measurement quadratic NLE reached values up to -0.5% and slowly decreased to -0.2% due to a degradation of the solar tracker mirrors, translating to a shift towards lower PTP values in the time series. The nonlinearity characterizations were derived from a sample of measurements during 17 days and no cubic nonlinearity feature was found in the out-of-band region. The sample quadratic NLE is linearly dependent on I_{PTP} (Fig. 16(a)) which translates into a hyperbolic shape for the coefficients of the nonlinearity characterizations, see panel (b). There is no cubic nonlinearity feature in the out-of-band region. The individual nonlinearity characterizations were then used to correct the interferograms (panel (c) shows the reduction in the quadratic

https://doi.org/10.5194/egusphere-2026-1890
Preprint. Discussion started: 14 April 2026

NLE). The difference in DMFs (corrected minus original) produced by the PROFFAST processor are shown in Fig. 16(d) reaching -0.2 ppm for xCO_2. For methane the DMF difference reaches -1.4 ppb for the interferograms with the higher PTP values. Both are below the reported COCCON systematic uncertainties: 0.63 ppm for xCO_2 and 6.3 ppb for xCH_4 (Herkommer et al., 2025).

5.3 Nonlinearity in TCCON measurements from the IFS 125HR instrument at Saint-Denis

The next two examples show two episodes for the TCCON Saint-Denis instrument when the instrument was affected by a strong nonlinearity with a nonzero cubic contribution. Similar to the previous examples we start with the individual nonlinearity characterizations obtained from a sample of measurements for each episode separately. This is illustrated in Figs. 17 and 19: panels (c) contain the estimates for a, b and panels (d) contain the coefficients of the individual characterizations. From the algorithm description in Sect. 2.4 we already know that the cubic coefficient estimate for this particular instrument setup relies on fitting a weak feature in the out-of-band region. This leads to more noise: panel (c) shows that cubic coefficient estimates have a higher spread compared to the quadratic coefficients and panel (d) shows that the higher noise is propagated to all orders for polynomial coefficients of the nonlinearity characterizations. When applying the TCCON GGG2020 processor (Laughner et al., 2024) on the nonlinearity corrected interferograms, the noise in the individual nonlinearity characterizations propagates to an unacceptable increased noise in the DMF gas retrievals. This is different from the previous COCCON example where, for the same optical setup, no cubic artifact was present and individual nonlinearity characterizations could be used. This higher sensitivity of the DMF retrievals to the noise in the cubic coefficients is also related to the cubic autocorrelation having a higher intensity in the in-band region compared to the quadratic autocorrelation (see Fig. 10).

To lower the noise in the cubic coefficients, we introduce a fitting procedure through the individual nonlinearity characterizations p_{DC}^{-1}. The outcome of this procedure is a *nonlinearity model*, i.e. a finite number of functions $a'(I_{\mathrm{PTP}}), b'(I_{\mathrm{PTP}}), \ldots$ that allow to obtain a nonlinearity characterization for an arbitrary interferogram I_m with PTP-property I_{PTP}. The nonlinearity characterization then takes the form $x + a'(I_{\mathrm{PTP}})x^2 + b'(I_{\mathrm{PTP}})x^3 + c'(I_{\mathrm{PTP}})x^4 + \cdots$ and can be used to correct the given interferogram. In the examples below the nonlinearity model functions are obtained from a polynomial fit through the NLEs of a sample of measurement.

5.3.1 A nonlinearity regime caused by detector saturation from the TCCON Saint-Denis site

The individual polynomial coefficients for p and p_{DC}^{-1} are calculated for a sample of three days during the April - May 2016 episode. From Fig. 17(a), showing the PTP-dependence of the quadratic coefficients, we can distinguish two nonlinearity subregimes separating morning and afternoon measurements. These subregimes are related to a change in the performance of the solar tracking in the morning and afternoon and are treated separately. In what follows, we focus on the afternoon (pm) measurements. The NLEs A and B in panel (b) are less noisy and reveal a nonlinear dependency on I_{PTP}. Using a LSQ fitting algorithm, a polynomial $A(I_{\mathrm{PTP}}) = c_4 I_{\mathrm{PTP}}^4 + c_3 I_{\mathrm{PTP}}^3$ is fitted through the sample quadratic NLE and a monomial $B(I_{\mathrm{PTP}}) = c_3 I_{\mathrm{PTP}}^3$ through the cubic NLE. The corresponding polynomial functions for the a, b coefficients are $a(I_{\mathrm{PTP}}) = 2A(I_{\mathrm{PTP}})/I_{\mathrm{PTP}}$ and $b(I_{\mathrm{PTP}}) = 4B(I_{\mathrm{PTP}})/I_{\mathrm{PTP}}^2$. These functions are also shown in panels (b) and (c) in Fig. 17. The trailing term in the fit

https://doi.org/10.5194/egusphere-2026-1890
Preprint. Discussion started: 14 April 2026

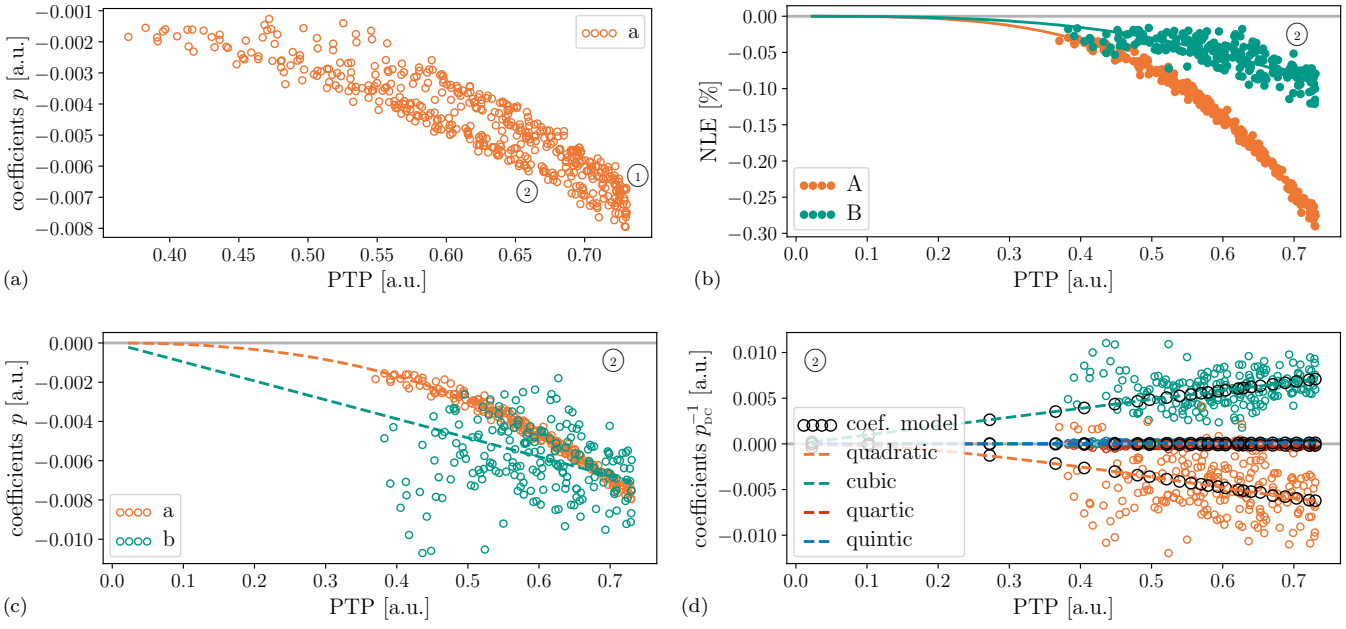

Figure 17. Nonlinearity regime at Saint-Denis during April 24 - May 23 2016 for a sample of measurements during three days. (a) The PTP-dependence of the quadratic coefficient a shows a different behavior during the morning (1) and afternoon (2) measurements. (b) A and B NLEs for the pm-measurements. The fitted functions $A(I_{\text{PTP}})$ and $B(I_{\text{PTP}})$ are shown in solid lines. (c) Similar as (b) but for the sample a, b coefficients. The fitted functions $a(I_{\text{PTP}})$ and $b(I_{\text{PTP}})$ are shown in dashed lines. (d) Similar as (b) but for the coefficients of the individual characterizations p_{DC}^{-1}. Dashed lines represent the nonlinearity model. The sample coefficients for the DC-shifted polynomials p_{PTP}^{-1} are indicated with black circles (quartic and quintic coefficients are close to zero and overlap).

polynomials for A and B was chosen to have degree three, sufficiently high to ensure that $a(I_{\text{PTP}})$ does not change sign close to the origin. Due to the higher noise level in the cubic coefficients B and to avoid any overfitting, the LSQ-fit is limited to a single coefficient (a monomial) and $b(I_{\text{PTP}})$ becomes a line through the origin.

The next step in the definition of a nonlinearity model is to take the coefficients functions $a(I_{\text{PTP}})$ and $b(I_{\text{PTP}})$ to coefficient functions for p_{DC}^{-1} following the algorithm steps 4 and 5 from Fig. 12. We did not attempt to do this analytically; instead we introduce a second LSQ fitting through a new set of coefficients: for each interferogram in the sample, with PTP-property I_{PTP}, DC-level d_c and polynomial $p_{\text{PTP}}(x) = x + a(I_{\text{PTP}})x^2 + b(I_{\text{PTP}})x^3$, we calculate the coefficients of the inverted and DC-shifted polynomial $p_{\text{PTP}}^{-1}(x - d_c)$. For each order separately these new coefficients (shown as black circles in panel (d) in Fig. 17) will be used in the final step of the definition of the nonlinearity model as an "average" for the sample individual nonlinearity characterizations, they smoothly depend on I_{PTP} and contain nearly no noise. The coefficient functions $a'(I_{\text{PTP}}), b'(I_{\text{PTP}}), \ldots$ for the nonlinearity model are obtained from a LSQ fit through these new coefficients for each order separately. The fit polynomial can be given more degrees of freedom and we have used $c'_8 I_{\text{PTP}}^8 + \cdots + c'_2 I_{\text{PTP}}^2 + c'_1 I_{\text{PTP}}$ (a constant term is absent to ensure intersection at the origin). The model coefficient functions are shown in Fig. 17(d) (dashed lines) and take the following form

https://doi.org/10.5194/egusphere-2026-1890
Preprint. Discussion started: 14 April 2026

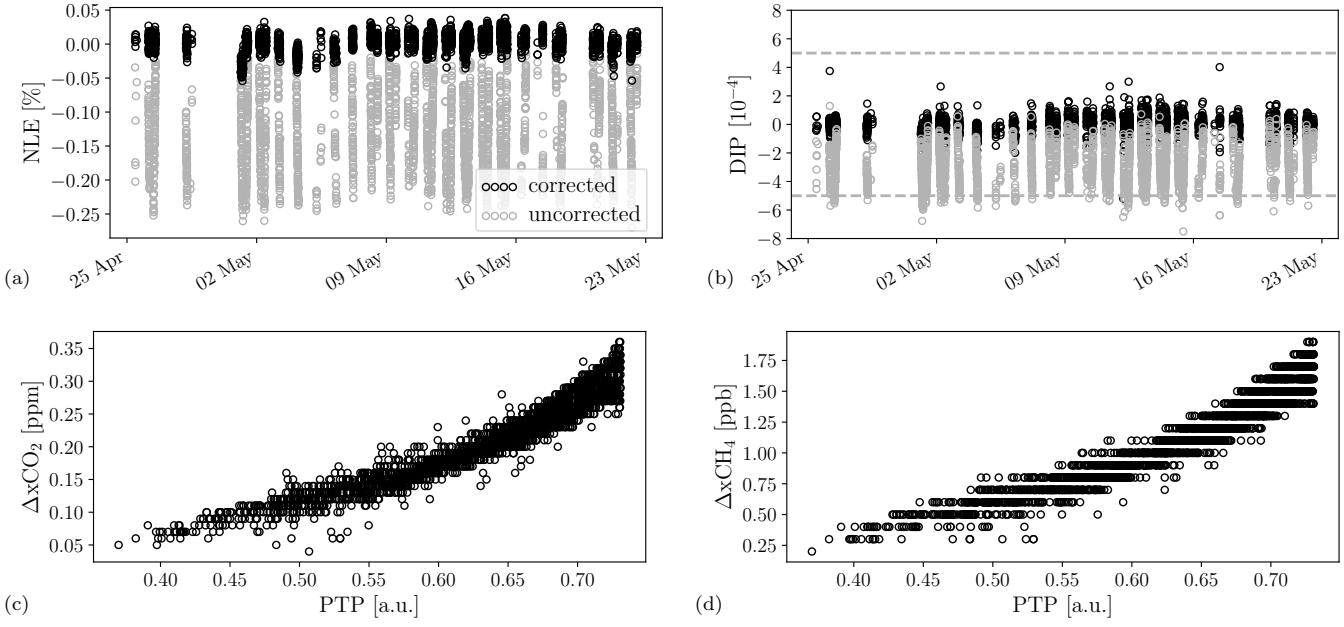

Figure 18. Nonlinearity correction for Saint-Denis during April - May 2016 using the model presented in Fig. 17. (a) Quadratic NLE reduction before and after correction. (b) Similar as (a) but for DIP, horizontal dashed lines show the TCCON reference thresholds on a running mean. (c) Difference in xCO_2 (nonlinearity corrected minus uncorrected DMF). (d) Similar as (c) but for xCH_4.

(up to the quintic coefficient, higher order terms are negligible)

$$a'(I_{\mathrm{PTP}}) = 5.77 I_{\mathrm{PTP}}^8 + \cdots + 1.58\ 10^{-1} I_{\mathrm{PTP}}^2 - 7.57\ 10^{-3} I_{\mathrm{PTP}},$$

$$\vdots$$

$$d'(I_{\mathrm{PTP}}) = -5.59\ 10^{-4} I_{\mathrm{PTP}}^8 + \cdots + 2.82\ 10^{-4} I_{\mathrm{PTP}}^2 - 8.31\ 10^{-8} I_{\mathrm{PTP}}.$$

This model was used on the Saint-Denis TCCON afternoon measurements to correct the nonlinearity. A similar model was constructed for the morning measurements. The effect on the TCCON retrievals is shown in Fig. 18. DIP and quadratic NLE estimates are significantly reduced and the effect on the DMF is of the order of 0.3 ppm for xCO_2 and 1.5 ppb for xCH_4. The TCCON uncertainty is estimated at 0.5 ppm for xCO_2 and 4.5 ppb for xCH_4 (Laughner et al., 2024).

5.3.2 A nonlinearity regime caused by optical misalignment from the TCCON Saint-Denis site

A second nonlinearity regime occurred at Saint-Denis during October 2013 until December 2014 and was caused by an optical misalignment related to inhomogeneous detector illumination; over-/underfilling of the detector element are known to create nonlinear response (Corredera et al., 2003; Laughner et al., 2024). The period under consideration is additionally characterized by a slow degradation in the solar tracker mirrors causing a shift from high to low PTP values. Similar to the previous regime, a sample of measurements is selected and the estimated coefficients are shown in panel (a) of Fig. 19. Two subregimes or

https://doi.org/10.5194/egusphere-2026-1890
Preprint. Discussion started: 14 April 2026

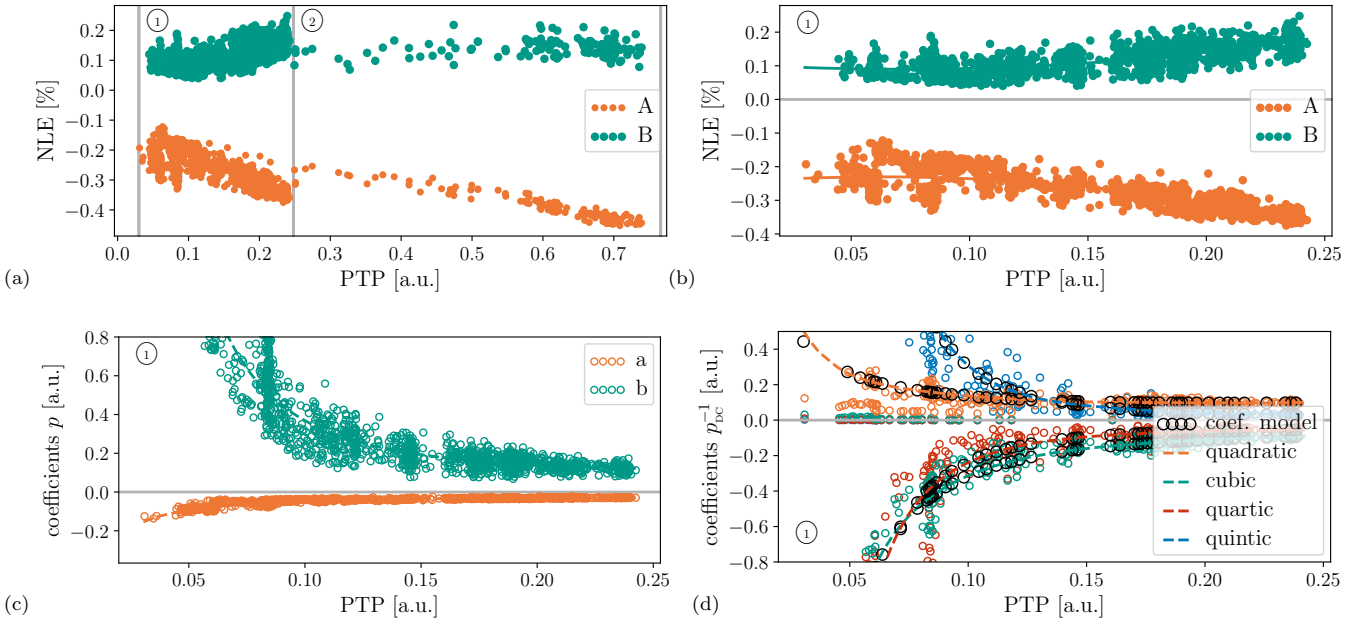

Figure 19. Nonlinearity regime at Saint-Denis during Oct. 2013 - Dec. 2014 obtained from a sample of nine days. (a) Sample NLEs values reveals two subregimes due to a clear step in the quadratic NLE at $I_{\mathrm{PTP}} = 0.25$. This was caused by a change in the instrument aperture: the first region covers the lower values up to $I_{\mathrm{PTP}} = 0.25$ and coincides with measurements mostly in 2014 with aperture 0.5 mm. The second period coincides with the higher values and coincides mostly with Oct.-Nov. 2013 with aperture 0.8 mm. (b)-(d) Similar as Fig. 17 showing the first period with 0.5 mm aperture. The coefficients $a(I_{\mathrm{PTP}})$ and $b(I_{\mathrm{PTP}})$ in (c) have a hyperbolic shape.

nonlinearity models should be considered due to a change in aperture settings for the instrument (from 0.8 mm in 2013 to 0.5 mm in 2014). Panels (b)-(d) in Fig. 19 consider the measurements with 0.5 mm aperture. The scaling-invariant coefficients A, B in panel (b) show a dominantly linear behavior with a nonzero intercept. A quadratic polynomial $c_2 I_{\mathrm{PTP}}^2 + c_1 I_{\mathrm{PTP}} + c_0$ was used to obtain a model for $A(I_{\mathrm{PTP}})$ and $B(I_{\mathrm{PTP}})$. In contrast to the saturation nonlinearity regime, the corresponding functions $a(I_{\mathrm{PTP}})$ and $b(I_{\mathrm{PTP}})$ show a hyperbolic dependency. The nonlinearity model coefficient functions are obtained in an analogous way as before: from a LSQ fitting through the smoothly varying sample coefficients for $p_{\mathrm{PTP}}^{-1}(x - d_c)$ obtained from the functions $A(I_{\mathrm{PTP}})$ and $B(I_{\mathrm{PTP}})$. Here a hyperbolic shaped polynomial of the form $c'_5 I_{\mathrm{PTP}}^5 + \cdots + c'_2 I_{\mathrm{PTP}}^2 + c'_1 I_{\mathrm{PTP}} + c'_0 + c'_{-1} I_{\mathrm{PTP}}^{-1} + c'_{-2} I_{\mathrm{PTP}}^{-2}$ was used. A similar model can be used for the measurements with 0.8 mm aperture.

After correction, the DIP satisfies the TCCON quality thresholds and the effect on the TCCON DMF is of the order of -0.5 ppm for xCO_2 and -2.5 ppb for xCH_4 (Fig. 20).

5.3.3 Comparison with the standardized TCCON nonlinearity correction approach

The concept of a nonlinearity model obtained by "averaging" individual nonlinearity characterizations was presented previously in Sha et al. (2020) to correct nonlinearity for the Sodankylä instrument. It is currently part of the TCCON pub-

https://doi.org/10.5194/egusphere-2026-1890
Preprint. Discussion started: 14 April 2026

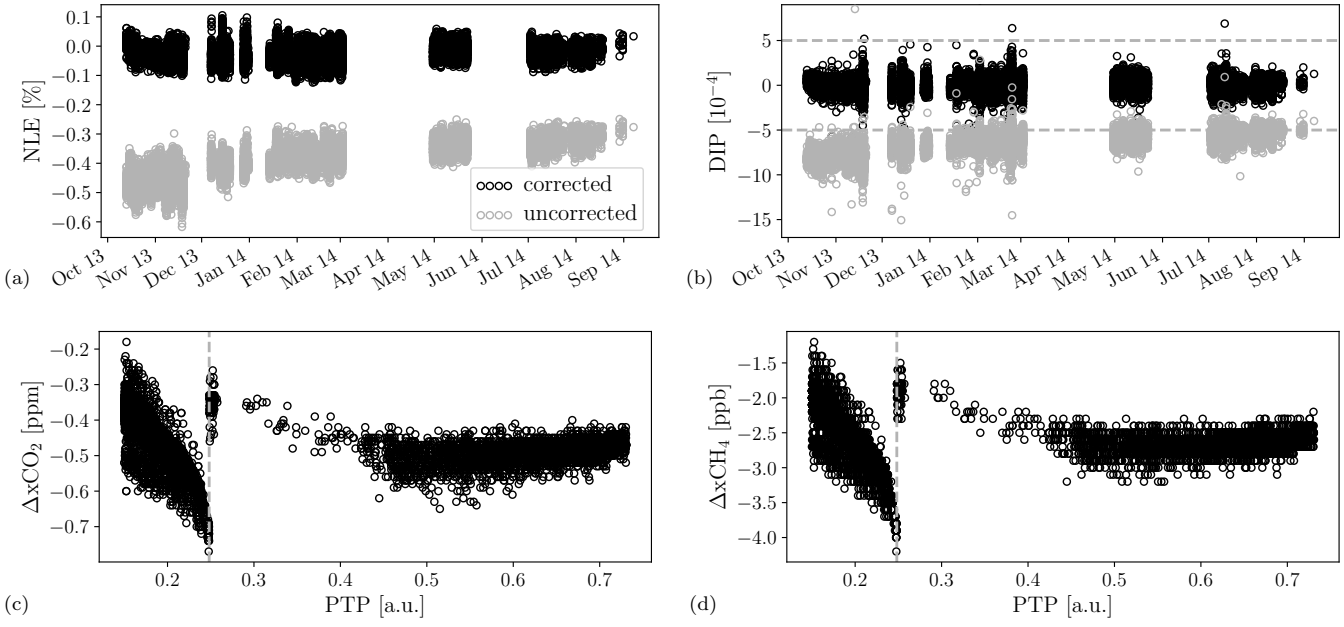

Figure 20. Similar as Fig. 18 for the period Oct. 2013 - Sept. 2014 and using the model presented in Fig. 19, leaving out the measurements with PTP below 0.15 with a high noise level in the retrieved DMF columns. The vertical line separates the two subregimes with different apertures.

lic software repository with the aim to incorporate it as a standardized part of the interferogram-to-spectrum processing in GGG2020 (Heikkinen and Kivi, 2023; Buschmann, 2023; Laughner et al., 2024).

The standardized TCCON approach shows some similarities with our nonlinearity model method: it determines individual nonlinearity characterizations for a sample of measurements from which a nonlinearity characterization is derived that is representative for a larger group of measurements.

There are two important differences between the standardized TCCON approach and the method presented in this paper. Firstly, in the TCCON approach the individual nonlinearity characterizations are obtained from a randomized optimization algorithm which varies the coefficients of a fourth order nonlinearity characterization to find a solution that minimizes the sum of the spectral amplitudes in the out-of-band region. The minimization algorithm restricts its domain of possible coefficients to non-negative coefficients $a', b', c' \geq 0$. This condition excludes the nonlinearity characterizations we derived for the Saint-Denis examples in panels (d) in Figures 17 and 19 where quadratic, cubic, quartic coefficients switch sign depending on the order. Secondly, the TCCON approach derives a single set of coefficients a', b', c' out of the sample of individual nonlinearity characterizations. For the nonlinearity models presented in the previous examples, we found that the coefficients are not constant, i.e. they depend on the PTP-property of an interferogram.

We briefly discuss three examples where we can compare the outcome of the two nonlinearity correction methods: a day in 2017 for the Sodankylä instrument, a day for the Xianghe instrument and one week for the TCCON candidate instrument

https://doi.org/10.5194/egusphere-2026-1890
Preprint. Discussion started: 14 April 2026

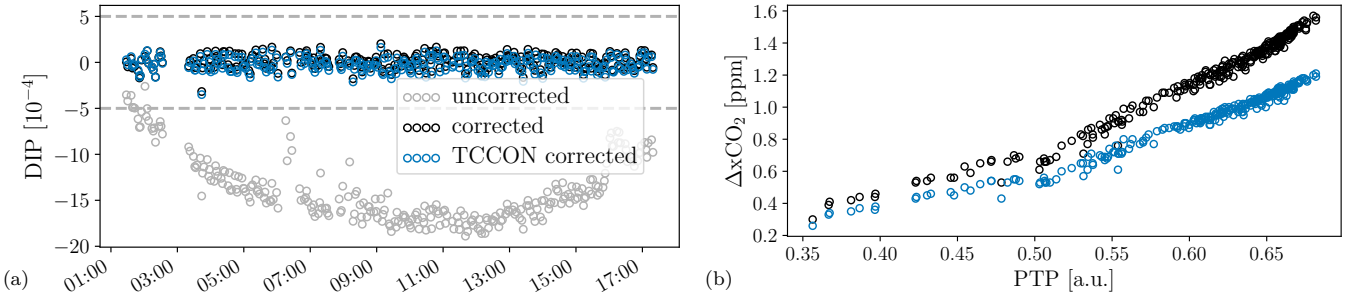

Figure 21. Nonlinearity correction methods for the Sodankyla TCCON instrument during 15 May 2017. (a) The DIP-diagnostic reduction for two nonlinearity models: the proposed method (black) and the standardized TCCON method (blue). Horizontal lines indicate the TCCON quality thresholds. (b) The difference in xCO_2 (corrected minus uncorrected) for the two nonlinearity correction methods.

in Kolkata with positive DIP. A nonlinearity model similar to the Saint-Denis saturation model in Fig. 17 was found for the Sodankylä measurements: they show a similar nonlinear dependence in the A and B coefficients. Although the coefficients from the nonlinearity model differ significantly from those obtained with the standardized TCCON approach, the nonlinearity model corrects the DIP to the same level but the effect on the Sodankylä DMFs is stronger: Fig. 21 shows the effect of the correction in xCO_2 reaches 1.2 ppm with the standardized TCCON approach and 1.6 with the proposed approach. This difference in xCO_2 between both approaches is comparable to the reported uncertainty. The difference in the corrected DMFs can bet related to the difference in the nonlinearity characterizations for the two approaches: the TCCON approach returns an optimal (minimizing out-of-band artifacts) polynomial within a constraint search domain but is arbitrary otherwise, while the new method imposes no constraint and fits out-of-band features using Eq. (2).

A nonlinearity model for the Xianghe TCCON instrument (Zhou et al., 2022) matches the PTP dependence seen in the Kolkata example: there is no cubic artifact and a dominantly linear dependence in A with a non-zero intercept. In this case the standardized TCCON nonlinearity coefficients were found to be in agreement with those produced by our nonlinearity model; only for interferograms with low PTP (low signal) the coefficients differ. Both approaches agree because the nonlinearity characterizations for this type of nonlinearity regime only contain positive coefficients (as in Fig. 16(b)) and coincide with the optimization domain of the TCCON approach. Note that, similar to the Saint-Denis 2013 regime, the Xianghe nonlinearity could be resolved after an optical re-alignment of the instrument. Nonlinearity models were set up for the candidate TCCON instruments in Porto Velho (Brazil) and Kolkata (India): they show a linear dependence in the NLEs A and B but with a positive quadratic NLE or DIP. The standardized TCCON approach was found to be ineffective in this situation (Laughner et al., 2024). Figure 22 shows the non-linearity model and the DIP diagnostic for the Kolkata spectra. The ΔxCO_2 (difference DMF obtained from nonlinearity corrected interferograms minus uncorrected) is on average 0.9 ppm. This nonlinearity model was set up for the measurements during the first seven days following the installation of the IFS 125HR in 2026. After an optical re-alignment, the DIP diagnostic reduced from 8×10^{-4} to an average value of 6×10^{-4}, which still exceeds the TCCON threshold. A new model should be defined for the period following this re-alignment to meet the TCCON requirements.

https://doi.org/10.5194/egusphere-2026-1890
Preprint. Discussion started: 14 April 2026

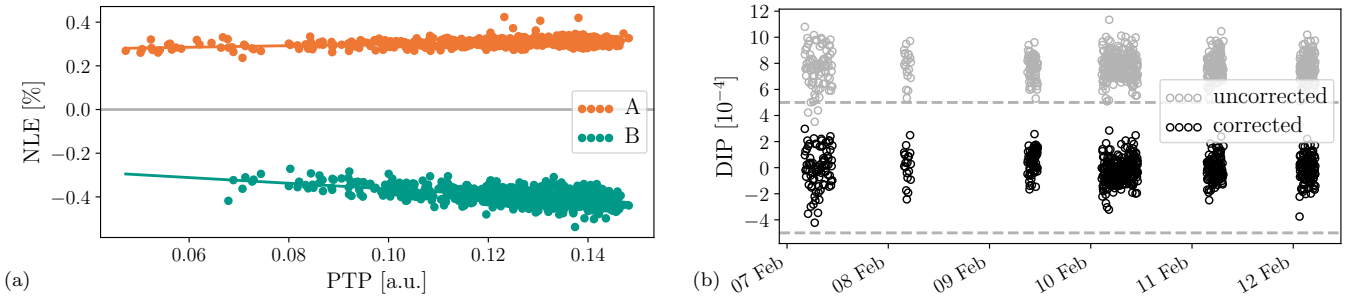

Figure 22. Nonlinearity regime at Kolkata during seven days in February 2026. (a) The scale-invariant coefficients from which the nonlinearity model is obtained. (b) The TCCON DIP diagnostic for the uncorrected and nonlinearity corrected interferograms. Horizontal lines indicate the TCCON quality thresholds.

6 Conclusions

A new nonlinearity characterization and correction method is presented and applied to groundbased solar absorption FTIR measurements obtained in the framework of the NDACC, TCCON or COCCON. The method uses the out-of-band spectral artifacts caused by nonlinear detector response and builds upon the methodology from Knuteson et al. (2004). It allows to estimate the coefficients of a polynomial that can be applied to the measured interferogram in order to obtain a nonlinearity corrected interferogram. The main advantages of the method are: it allows to correct for different higher order nonlinearity artifacts at once; it is applicable for all detectors used in the three networks (InGaAs, InSb and MCT); it is applicable to both AC and DC recorded interferograms; it allows to correct negative and positive DIP; it requires no external input such as calibration measurements; it contains an uncertainty estimation on the fitted polynomial coefficients. Although the proposed algorithm assumes the corrected spectra do not require an absolute calibration, parts of the proposed method are believed to be relevant in that context.

To apply the algorithm most efficiently, the user should investigate the out-of-band region and select appropriate subwindows containing the spectral artifacts caused by nonlinear detector response. This manual effort should only be done once per optical instrument setup and should be applicable to all instruments in a network that share the same optical setup. Three examples were discussed to demonstrate how this subwindow selection can be done by means of the in-band spectrum autocorrelations and by taking into account the complex phase of the measured spectrum in the out-of-band region.

Limitations and robustness of the algorithm were discussed in detail. Key limitations are: the out-of-band spectral artifacts may not overlap with other artifacts such as ghosts; higher order nonlinearity artifacts, if present, should not completely overlap with each other (the signal of quadratic and cubic features in the out-of-band region should be separable); the interferograms should be recorded with a sufficiently large out-of-band region (interferogram undersampling should be limited); very strong nonlinearity episodes are out-of-scope because the out-of-band and in-band regions are distorted too heavily and spectral signals of the autocorrelations in the polynomial expansion are not distinguishable.

https://doi.org/10.5194/egusphere-2026-1890
Preprint. Discussion started: 14 April 2026

The method was developed and tested using spectra from several instruments: Sodankyla (NDACC and TCCON), Bremen (NDACC), Xianghe (NDACC and TCCON), Kolkata (COCCON and TCCON), Porto-Velho (NDACC and TCCON) and Saint-Denis (TCCON). From these time series four different episodes were selected during which measurements were affected by detector nonlinearity. Each episode was discussed in detail and for each the effect of the nonlinearity correction on the retrieved columns (total column or DMF) was compared to the reported column uncertainty. The effect of nonlinearity correction for the COCCON and TCCON standard network processor (PROFFAST and GGG2020 resp.) can cause corrections that exceed the reported column uncertainties. For the NDACC retrieval strategies a similar conclusion holds. However, the SFIT4 processor allows to co-retrieve parameters that can correct the nonlinearity induced spectral baseline offset in the in-band region. This is the case in e.g. the ACTRIS ozone retrieval strategy where the effect of nonlinearity correction was shown to be negligible. For the sake of completeness, we should mention that the second NDACC processor PROFFIT was not part of this study (Hase et al., 2004).

The proposed method was compared to the standardized TCCON nonlinearity correction approach. The method was applied on TCCON measurements showing a positive DIP, a case where the standardized TCCON approach was known to be ineffective. Depending on the underlying nonlinearity regime, the two approaches can deviate and produce a different effect on the TCCON retrieved DMFs after correction. New metrics for nonlinearity error NLE were introduced and they represent the relative error on the true interferogram at ZOPD caused by the (dominant) quadratic nonlinearity artifact and higher order artifacts. In the episodes considered we found that these nonlinearity metrics either show a dominantly linear or higher order dependency on the interferogram peak-to-peak-property PTP near the center burst. A higher order (biquadratic) dependency could be related to nonlinearity episodes caused by detector saturation while a linear dependency with a nonzero intercept could be related to an instrument optical misalignment. More episodes should be studied to confirm the link between the shape of the PTP-NLE relationship and the cause of the detector nonlinearity.

Code availability. The python code used to analyze the interferograms is available at https://doi.org/10.18758/PPEQABK9, Langerock (2026).

Author contributions. BL did the conceptualization, the formal analysis, methodology, software development, visualization and the writing of the initial draft of the published work. MZ provided resources in running the GGG2020 processor on the Xianghe measurements and investigated the nonlinearity aspects of the Xianghe spectra. MKS and FD provided funding and resources in running the GGG2020 processor on the Saint-Denis measurements and the PROFFAST processor on the Kolkata measurements and investigated the nonlinearity aspects of these spectra, in particular the interpretation of the TCCON and COCCON results and investigation of the cause of the nonlinearity regimes. CV and BD provided resources in the development and application of the NDACC/ACTRIS ozone retrieval strategy and investigated the nonlinearity aspects on these data products. MP provided resources in the provision of the Bremen measurements and the application of the NDACC/ACTRIS ozone retrieval strategy. RK provided the TCCON measurements at Sodankylä. MDM provided funding and resources for the TCCON measurements at Saint-Denis, the NDACC measurements at Maïdo and the TCCON and COCCON data from Kolkata

https://doi.org/10.5194/egusphere-2026-1890
Preprint. Discussion started: 14 April 2026

and investigated the nonlinearity aspects in these spectra. MT, SR, GKB and SB maintained and supported the Vertex70 and IFS 125HR operations in Kolkata. IM provided funding and supported the installation and operation of the IFS 125HR at Kolkata. All authors read, reviewed and agreed to the published version of this work.

Competing interests. The authors declare that they have no conflict of interest.

Acknowledgements. The BELSPO ProDEx project TROVA-E2 (PEA 4000116692), SVANTE (4000132151/20/NL/FF/ab), FRM4GHG (4000117640/16/I-LG and 4000136108/21/I-DT-lr), and ACTRIS-BE (FSIRI/00/AC1 and EF/241/ACTRIS2BE) projects provided funding for the observations used in this work. The budget for the Kolkata FTIR site is partially funded by the GOSAT series project and partly by ESA SVANTE (4000132151/20/NL/FF/ab) and SVANTE II (4000147200/25/NL/FFi). The installation and operation of the FTIR at the Kolkata site is also supported in part by the GOSAT series project, SVANTE II project and local support by IISER-Kolkata. Nicolas Kumps, Tom Boonants and Christian Hermans for the instrument operations in Saint-Denis and Kolkata. Jean-Marc Metzger is acknowledged for the instrument operations at Maïdo and Saint-Denis. Carlos Augusto Bauer Aquino for the instrument operations at Portovelho and Caroline Jonas for the useful suggestions during the manuscript preparations.

https://doi.org/10.5194/egusphere-2026-1890
Preprint. Discussion started: 14 April 2026

References

Abrams, M. C., Toon, G. C., and Schindler, R. A.: Practical example of the correction of Fourier-transform spectra for detector nonlinearity, Appl. Opt., 33, 6307–6314, https://doi.org/10.1364/AO.33.006307, 1994.

Buschmann, M.: Standalone Python Qt program to provide live preview of the idle mode measurements of an IFS125HR, https://github.com/mbuschmann/ifs125preview, 2023.

Chase, D. B.: Nonlinear Detector Response in FT-IR, Appl. Spectrosc., 38, 491–494, https://opg.optica.org/as/abstract.cfm?URI=as-38-4-491, 1984.

Corredera, P., Hernanz, M. L., González-Herráez, M., and Campos, J.: Anomalous non-linear behaviour of InGaAs photodiodes with over-filled illumination, Metrologia, 40, S150, https://doi.org/10.1088/0026-1394/40/1/334, 2003.

De Mazière, M., Thompson, A. M., Kurylo, M. J., Wild, J. D., Bernhard, G., Blumenstock, T., Braathen, G. O., Hannigan, J. W., Lambert, J.-C., Leblanc, T., McGee, T. J., Nedoluha, G., Petropavlovskikh, I., Seckmeyer, G., Simon, P. C., Steinbrecht, W., and Strahan, S. E.: The Network for the Detection of Atmospheric Composition Change (NDACC): history, status and perspectives, Atmospheric Chemistry and Physics, 18, 4935–4964, https://doi.org/10.5194/acp-18-4935-2018, 2018.

De Mazière, M., Sha, M. K., Desmet, F., Hermans, C., Scolas, F., Kumps, N., Zhou, M., Metzger, J.-M., Duflot, V., and Cammas, J.-P.: TCCON data from Réunion Island (RE), Release GGG2020.R0, https://doi.org/10.14291/TCCON.GGG2020.REUNION01.R0, 2022.

Dohe, S., Sherlock, V., Hase, F., Gisi, M., Robinson, J., Sepúlveda, E., Schneider, M., and Blumenstock, T.: A method to correct sampling ghosts in historic near-infrared Fourier transform spectrometer (FTS) measurements, Atmospheric Measurement Techniques, 6, 1981–1992, https://doi.org/10.5194/amt-6-1981-2013, 2013.

Feld, L., Herkommer, B., Vestner, J., Dubravica, D., Alberti, C., and Hase, F.: PROFFASTpylot: Running PROFFAST with Python, Journal of Open Source Software, 9, 6481, https://doi.org/10.21105/joss.06481, 2024.

Forman, M. L., Steel, W. H., and Vanasse, G. A.: Correction of Asymmetric Interferograms Obtained in Fourier Spectroscopy∗, J. Opt. Soc. Am., 56, 59–63, https://doi.org/10.1364/JOSA.56.000059, 1966.

Frey, M., Sha, M. K., Hase, F., Kiel, M., Blumenstock, T., Harig, R., Surawicz, G., Deutscher, N. M., Shiomi, K., Franklin, J. E., Bösch, H., Chen, J., Grutter, M., Ohyama, H., Sun, Y., Butz, A., Mengistu Tsidu, G., Ene, D., Wunch, D., Cao, Z., Garcia, O., Ramonet, M., Vogel, F., and Orphal, J.: Building the COllaborative Carbon Column Observing Network (COCCON): long-term stability and ensemble performance of the EM27/SUN Fourier transform spectrometer, Atmospheric Measurement Techniques, 12, 1513–1530, https://doi.org/10.5194/amt-12-1513-2019, 2019.

Guo, Q., Liu, Y., Wang, X., and Hui, W.: A new non-linearity correction method for the spectrum from the Geostationary Inferometric Infrared Sounder on board Fengyun-4 satellites and its preliminary assessments, Atmospheric Measurement Techniques, 17, 4613–4627, https://doi.org/10.5194/amt-17-4613-2024, 2024.

Han, Y.: 7.08 - The Cross-Track Infrared Sounder Overview and Validation, in: Comprehensive Remote Sensing, edited by Liang, S., pp. 235–296, Elsevier, Oxford, ISBN 978-0-12-803221-3, https://doi.org/https://doi.org/10.1016/B978-0-12-409548-9.10392-6, 2018.

Hannigan, J., Palm, M., Jones, N., Ortega, I., Langerock, B., Mahieu, E., Zhou, M., and Smale, D.: SFIT4 Line-by-line nonlinear spectral fitting software: version 1.0.21, https://doi.org/10.18758/CLYG3EUO, 2024.

Harris, F.: On the use of windows for harmonic analysis with the discrete Fourier transform, Proceedings of the IEEE, 66, 51–83, https://doi.org/10.1109/PROC.1978.10837, 1978.

https://doi.org/10.5194/egusphere-2026-1890
Preprint. Discussion started: 14 April 2026

Hase, F.: Inversion von Spurengasprofilen aus hochaufgelösten bodengebundenen FTIR-Messungen in Absorption, Ph.D. thesis, https://doi.org/10.5445/IR/2752000, 22.02.11; LK 01; Fak. f. Physik, Diss. v. 14.7.2000., 2000.

Hase, F., Hannigan, J., Coffey, M., Goldman, A., Höpfner, M., Jones, N., Rinsland, C., and Wood, S.: Intercomparison of retrieval codes used for the analysis of high-resolution, ground-based FTIR measurements, Journal of Quantitative Spectroscopy and Radiative Transfer, 87, 25–52, https://doi.org/https://doi.org/10.1016/j.jqsrt.2003.12.008, 2004.

Heikkinen, P. and Kivi, R.: Nonlin5 software to correct nonlinearity in 125HR spectra, https://github.com/TCCON/nonlin5, 2023.

Herkommer, B., Hase, F., Groß, J., Alberti, C., Castracane, P., Dehn, A., Chen, J., Dietrich, F., Morino, I., Frey, M. M., Gillespie, L., Pak, N. M., Wunch, D., Deutscher, N., Walker, B., and García, O. E.: Using a portable EM27/SUN FTIR-spectrometer for validating the TCCON site-to-site consistency: The COCCON Travel Standard, https://doi.org/10.5194/egusphere-egu24-5350, 2025.

Herres, W. and Gronholz, J.: Understanding FT-IR data processing, Part 2, Intell. Instrum. Comput., Appl. Lab., 3, 10–19, 1984.

Keppel-Aleks, G., Toon, G. C., Wennberg, P. O., and Deutscher, N. M.: Reducing the impact of source brightness fluctuations on spectra obtained by Fourier-transform spectrometry, Appl. Opt., 46, 4774–4779, https://doi.org/10.1364/AO.46.004774, 2007.

Kivi, R., Heikkinen, P., and Kyrö, E.: TCCON data from Sodankylä (FI), Release GGG2020.R0, https://doi.org/10.14291/TCCON.GGG2020.SODANKYLA01.R0, 2022.

Knuteson, R. O., Revercomb, H. E., Best, F. A., Ciganovich, N. C., Dedecker, R. G., Dirkx, T. P., Ellington, S. C., Feltz, W. F., Garcia, R. K., Howell, H. B., Smith, W. L., Short, J. F., and Tobin, D. C.: Atmospheric Emitted Radiance Interferometer. Part II: Instrument Performance, Journal of Atmospheric and Oceanic Technology, 21, 1777 – 1789, https://doi.org/10.1175/JTECH-1663.1, 2004.

Lachance, R. L.: Non-linearity correction of FTIR instruments, Presented at the Fifth Workshop of Infrared Emission Measurements by FTIR, ABB Bomem, 2000.

Langerock, B.: Python package for FTIR interferogram and spectrum analysis, https://doi.org/10.18758/PPEQABK9, 2026.

Laughner, J. L., Toon, G. C., Mendonca, J., Petri, C., Roche, S., Wunch, D., Blavier, J.-F., Griffith, D. W. T., Heikkinen, P., Keeling, R. F., Kiel, M., Kivi, R., Roehl, C. M., Stephens, B. B., Baier, B. C., Chen, H., Choi, Y., Deutscher, N. M., DiGangi, J. P., Gross, J., Herkommer, B., Jeseck, P., Laemmel, T., Lan, X., McGee, E., McKain, K., Miller, J., Morino, I., Notholt, J., Ohyama, H., Pollard, D. F., Rettinger, M., Riris, H., Rousogenous, C., Sha, M. K., Shiomi, K., Strong, K., Sussmann, R., Té, Y., Velazco, V. A., Wofsy, S. C., Zhou, M., and Wennberg, P. O.: The Total Carbon Column Observing Network's GGG2020 data version, Earth System Science Data, 16, 2197–2260, https://doi.org/10.5194/essd-16-2197-2024, 2024.

McClellan, J., Schafer, R., and Yoder, M.: Digital Signal Processing First, Global Edition, Always learning, Pearson, ISBN 9781292113869, 2016.

Mertz, L.: Auxiliary computation for Fourier spectrometry, Infrared Physics, 7, 17–23, https://doi.org/https://doi.org/10.1016/0020-0891(67)90026-7, 1967.

Messerschmidt, J., Macatangay, R., Notholt, J., Petri, C., Warneke, T., and Weinzierl, C.: Side by side measurements of CO2 by ground-based Fourier transform spectrometry (FTS), Tellus B: Chemical and Physical Meteorology, https://doi.org/10.1111/j.1600-0889.2010.00491.x, 2010.

Moré, J. J.: The Levenberg-Marquardt algorithm: Implementation and theory, in: Numerical Analysis, edited by Watson, G. A., pp. 105–116, Springer Berlin Heidelberg, Berlin, Heidelberg, ISBN 978-3-540-35972-2, 1978.

Morse, P. M. and Feshbach, H.: Methods of Theoretical Physics. Vol. 1-2, McGraw-Hill, 1953.

https://doi.org/10.5194/egusphere-2026-1890
Preprint. Discussion started: 14 April 2026

Notholt, J., Toon, G., Jones, N., Griffith, D., and Warneke, T.: Spectral line finding program for atmospheric remote sensing using full radiation transfer, Journal of Quantitative Spectroscopy and Radiative Transfer, 97, 112–125, https://doi.org/https://doi.org/10.1016/j.jqsrt.2004.12.025, 2006.

Petropavlovskikh, I., De Mazière, M., Thompson, A. M., Wild, J. D., Hannigan, J. W., Selkirk, H. B., Hannum, R. A., Steinbrecht, W., Lambert, J.-C., Van Malderen, R., Asher, E., Cordero, R. R., Godin-Beekmann, S., Hubert, D., Khaykin, S., Kreher, K., Leblanc, T., Mahieu, E., Maillard Barras, E., McConville, G., Nedoluha, G., Ortega, I., Redondas Marrero, A., Seckmeyer, G., Stauffer, R. M., Strode, S. A., Strong, K., Sugita, T., Van Roozendael, M., Velazco, V., Vigouroux, C., and Vogel, B.: The Network for the Detection of Atmospheric Composition Change at 35 Years: Achievements and Future Strategy, EGUsphere, 2026, 1–52, https://doi.org/10.5194/egusphere-2025-6557, 2026.

Qi, C., Wu, C., Hu, X., Xu, H., Lee, L., Zhou, F., Gu, M., Yang, T., Shao, C., Yang, Z., and Zhang, P.: High Spectral Infrared Atmospheric Sounder (HIRAS): System Overview and On-Orbit Performance Assessment, IEEE Transactions on Geoscience and Remote Sensing, 58, 4335–4352, https://doi.org/10.1109/TGRS.2019.2963085, 2020.

Sha, M. K., De Mazière, M., Notholt, J., Blumenstock, T., Chen, H., Dehn, A., Griffith, D. W. T., Hase, F., Heikkinen, P., Hermans, C., Hoffmann, A., Huebner, M., Jones, N., Kivi, R., Langerock, B., Petri, C., Scolas, F., Tu, Q., and Weidmann, D.: Intercomparison of low- and high-resolution infrared spectrometers for ground-based solar remote sensing measurements of total column concentrations of CO_2, CH_4, and CO, Atmospheric Measurement Techniques, 13, 4791–4839, https://doi.org/10.5194/amt-13-4791-2020, 2020.

Sha, M. K., Das, S., Frey, M. M., Dubravica, D., Alberti, C., Baier, B. C., Balis, D., Bezanilla, A., Blumenstock, T., Boesch, H., Cai, Z., Chen, J., Dandocsi, A., Mazière, M. D., Foka, S., García, O., Gillespie, L. D., Gribanov, K., Gross, J., Grutter, M., Handley, P., Hase, F., Heikkinen, P., Humpage, N., Jacobs, N., Jeong, S., Karppinen, T., Kiel, M., Kivi, R., Langerock, B., Laughner, J., Lopez, M., Makarova, M., Mermigkas, M., Morino, I., Mostafavipak, N., Nemuc, A., Newberger, T., Ohyama, H., Okello, W., Osterman, G., Park, H., Pirloaga, R., Pollard, D. F., Raffalski, U., Ramonet, M., Sepúlveda, E., Simpson, W. R., Stremme, W., Sweeney, C., Taquet, N., Topaloglou, C., Tu, Q., Warneke, T., Wunch, D., Zakharov, V., and Zhou, M.: Fiducial Reference Measurements for Greenhouse Gases (FRM4GHG): Validation of Satellite (Sentinel-5 Precursor, OCO-2, and GOSAT) Missions Using the COllaborative Carbon Column Observing Network (COCCON), Remote Sensing, 17, https://doi.org/10.3390/rs17050734, 2025.

Vigouroux, C.: Ozone (O3) groundbased remote sensing data from the FTIR instrument BIRA.IASB003 at the Maido Observatory, version IRWG2023.CP, https://doi.org/10.60897/ndacc.la.reunion.maido_ftir.o3_bira.iasb003_irwg2023.cp, 2025.

Virtanen, P., Gommers, R., Oliphant, T. E., Haberland, M., Reddy, T., Cournapeau, D., Burovski, E., Peterson, P., Weckesser, W., Bright, J., van der Walt, S. J., Brett, M., Wilson, J., Millman, K. J., Mayorov, N., Nelson, A. R. J., Jones, E., Kern, R., Larson, E., Carey, C. J., Polat, İ., Feng, Y., Moore, E. W., VanderPlas, J., Laxalde, D., Perktold, J., Cimrman, R., Henriksen, I., Quintero, E. A., Harris, C. R., Archibald, A. M., Ribeiro, A. H., Pedregosa, F., van Mulbregt, P., and SciPy 1.0 Contributors: SciPy 1.0: Fundamental Algorithms for Scientific Computing in Python, Nature Methods, 17, 261–272, https://doi.org/10.1038/s41592-019-0686-2, 2020.

Weisstein, E. W.: Series Reversion. From MathWorld–A Wolfram Resource. https://mathworld.wolfram.com/SeriesReversion.html, 2026.

Wunch, D., Toon, G. C., Blavier, J.-F. L., Washenfelder, R. A., Notholt, J., Connor, B. J., Griffith, D. W., Sherlock, V., and Wennberg, P. O.: The total carbon column observing network, Philosophical Transactions of the Royal Society of London A: Mathematical, Physical and Engineering Sciences, 369, 2087–2112, 2011.

Wunch, D., Toon, G. C., Sherlock, V., Deutscher, N. M., Liu, C., Feist, D. G., and Wennberg, P. O.: The Total Carbon Column Observing Network's GGG2014 Data Version, Tech. rep., Carbon Dioxide Information Analysis Cen-

https://doi.org/10.5194/egusphere-2026-1890
Preprint. Discussion started: 14 April 2026

ter, Oak Ridge National Laboratory, Oak Ridge, Tennessee, U.S.A. doi: 10.14291/tccon.ggg2014.documentation.R0/1221662, https://doi.org/10.14291/tccon.ggg2014.documentation.R0/1221662, 2015.

Zhou, M., Wang, P., Kumps, N., Hermans, C., and Nan, W.: TCCON data from Xianghe, China, Release GGG2020.R0, https://doi.org/10.14291/TCCON.GGG2020.XIANGHE01.R0, 2022.